



## Catalytic Carbon–Halogen Bond Activation: Trends in Reactivity, Selectivity, and Solvation

G. Theodoor de Jong and F. Matthias Bickelhaupt\*

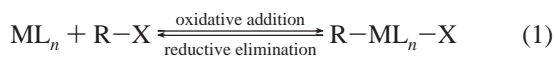
*Afdeling Theoretische Chemie, Scheikundig Laboratorium der Vrije Universiteit, De Boelelaan 1083, NL-1081 HV Amsterdam, The Netherlands*

Received November 22, 2006

**Abstract:** We have theoretically studied the oxidative addition of all halomethanes  $\text{CH}_3\text{X}$  (with  $\text{X} = \text{F}, \text{Cl}, \text{Br}, \text{I}, \text{At}$ ) to Pd and  $\text{PdCl}^-$ , using both nonrelativistic and zeroth-order-regular-approximation-relativistic density functional theory at BLYP/QZ4P. Our study covers the gas phase as well as the condensed phase (water), where solvent effects are described with the conductor-like screening model. The activation of the  $\text{C}^*-\text{X}$  bond may proceed via two stereochemically different pathways: (i) direct oxidative insertion (OxIn) which goes with *retention* of the configuration at  $\text{C}^*$  and (ii) an alternative  $\text{S}_{\text{N}}2$  pathway which goes with *inversion* of the configuration at  $\text{C}^*$ . In the gas phase, for Pd, the OxIn pathway has the lowest reaction barrier for all  $\text{CH}_3\text{X}$ 's. Anion assistance, that is, going from Pd to  $\text{PdCl}^-$ , changes the preference for all  $\text{CH}_3\text{X}$ 's from OxIn to the  $\text{S}_{\text{N}}2$  pathway. Gas-phase reaction barriers for both pathways to  $\text{C}-\text{X}$  activation generally decrease as X descends in group 17. Two striking solvent effects are (i) the shift in reactivity of  $\text{Pd} + \text{CH}_3\text{X}$  from OxIn to  $\text{S}_{\text{N}}2$  in the case of the smaller halogens, F and Cl, and (ii) the shift in reactivity of  $\text{PdCl}^- + \text{CH}_3\text{X}$  in the opposite direction, that is, from  $\text{S}_{\text{N}}2$  to OxIn, in the case of the *heavier* halogens, I and At. We use the activation strain model to arrive at a qualitative understanding of how the competition between OxIn and  $\text{S}_{\text{N}}2$  pathways is determined by the halogen atom in the activated  $\text{C}-\text{X}$  bond, by anion assistance, and by solvation.

### 1. Introduction

Oxidative addition and reductive elimination (eq 1) are ubiquitous as elementary reaction steps in homogeneous catalysis<sup>1–3</sup> and have been intensively investigated both experimentally<sup>3–5</sup> and theoretically.<sup>5–14</sup>

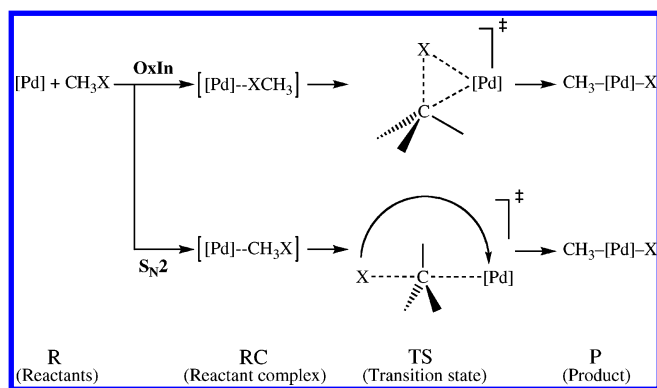


A well-known class of processes involving oxidative addition is catalytic  $\text{C}-\text{X}$  bond activation.<sup>1,15</sup> The catalytically active species in these reactions are generally coordination complexes of palladium or other transition metals. This process is an efficient tool for selectively converting simple educts, via  $\text{C}-\text{C}$  bond formation, into more complex compounds

and is therefore of major importance for synthetic chemistry. The most intensively used substrates for such  $\text{C}-\text{C}$  coupling reactions are aryl halides, whereas it is more difficult in this context to exploit alkyl halides.<sup>16</sup>

In the oxidative addition process, the metal increases its formal oxidation state by two units. There has been controversy about the mechanism of this reaction, notably concerning the  $\text{C}-\text{Cl}$  bond.<sup>17</sup> One mechanism that has been proposed requires the concerted transfer of two electrons and involves either a concerted front-side displacement or a concerted nucleophilic displacement ( $\text{S}_{\text{N}}2$ ) proceeding via backside attack of the  $\text{C}-\text{Cl}$  bond by the metal. Theoretical studies on the oxidative addition of the  $\text{C}-\text{Cl}$  bond in chloromethane to the Pd atom in the gas phase show that this process can indeed proceed via direct oxidative insertion of the metal into the  $\text{C}-\text{Cl}$  bond (OxIn) or via  $\text{S}_{\text{N}}2$  substitution followed, in a concerted manner, by leaving-group rearrangement ( $\text{S}_{\text{N}}2$ -

\* Corresponding author fax: +31-20-5987629; e-mail: fm.bickelhaupt@few.vu.nl.

**Scheme 1.** Model Reactions and Nomenclature

ra).<sup>10,14,18</sup> The reaction barrier for OxIn is lower than that for the  $S_N2$  pathway. Interestingly, anion assistance, for example, coordination of a chloride anion to Pd, reverses this order in activation energies and makes  $S_N2$  the preferred pathway. Note that this shift in mechanism also corresponds to a change in stereochemistry at the carbon atom involved, namely, from retention (OxIn) to inversion of the configuration ( $S_N2$ ). This is of practical relevance for substrates in which the carbon atom,  $C^*$ , is asymmetric (which is obviously not the case in the simple model substrate chloromethane). The two pathways are schematically summarized in Scheme 1.

In the present study, we aim at obtaining insight into the trends in reactivity of palladium and all possible carbon–halogen bonds, that is,  $C-X$ , with  $X = F, Cl, Br, I$ , and  $At$ . Along this series of halogens, we are particularly interested in the preference for one of the two pathways, OxIn or  $S_N2$ , and how this preference is affected by three different aspects, namely, (i) anion assistance, that is, using  $PdCl^-$  instead of  $Pd$ , (ii) relativistic effects, and (iii) solvent effects, in particular, changing from the gas phase to an aqueous solution. To this end, we have calculated a set of consistent potential energy surfaces (PESs), using both nonrelativistic and relativistic density functional theory (DFT) and, for the solvent effects, using a continuum solvation model, which enables us to infer accurate trends in reactivity for these simple, archetypal oxidative addition reactions.

The differences in reactivity for the various combinations of inserting metal complexes, namely, bare  $Pd$  and  $PdCl^-$ , and substrates  $CH_3X$  are analyzed and interpreted in terms of the activation strain model of chemical reactivity.<sup>7,9,10,19</sup> In this model, activation energies  $\Delta E^\ddagger$  are decomposed into the activation strain  $\Delta E_{\text{strain}}^\ddagger$  of and the stabilizing transition state (TS) interaction  $\Delta E_{\text{int}}^\ddagger$  between the reactants in the activated complex:  $\Delta E^\ddagger = \Delta E_{\text{strain}}^\ddagger + \Delta E_{\text{int}}^\ddagger$ . The activation strain  $\Delta E_{\text{strain}}^\ddagger$  depends on the strength of the activated bond and on the extent to which a particular metal expands the bond in the activated complex. The TS interaction  $\Delta E_{\text{int}}^\ddagger$  is directly determined by the bonding capabilities and, thus, the frontier orbitals of the reactants. As will emerge from our analyses, much of the trends in reaction characteristics can be traced to the different strengths of the carbon–halogen bonds and the energy levels of the highest occupied and lowest unoccupied molecular orbitals (HOMO and LUMO, respectively) in the substrates.

## 2. Computational Methods

**2.1. DFT Calculations.** All DFT<sup>20</sup> calculations have been done with the Amsterdam Density Functional (ADF) program.<sup>21,22</sup> Calculations were done either nonrelativistically or with scalar relativistic effects accounted for using the zeroth-order regular approximation (ZORA).<sup>23</sup> For the dissociation energies of the  $C-X$  bonds, where spin–orbit coupling is expected to be important, also single-point calculations using double-group symmetry including spin–orbit effects were done. The BLYP<sup>24</sup> density functional was used, in combination with the QZ4P basis set for all elements except hydrogen, for which the TZ2P basis set was used. The QZ4P basis set is a large uncontracted set of Slater-type orbitals (STOs) containing diffuse functions. It is of quadruple- $\zeta$  quality and has been augmented with several sets of polarization functions on each atom: two 3d and two 4f sets on F, three 3d and two 4f sets on Cl, two 4d and three 4f sets on Br, one 5d and three 4f sets on I, one 6d and two 5f sets on At, two 3d and two 4f sets on C, and two 5p and two 4f sets on Pd. The TZ2P basis set, only used for hydrogen, is of triple- $\zeta$  quality and has been augmented with two sets of polarization functions: 2p and 3d in the case of H. An auxiliary set of s, p, d, f, and g STOs was used to fit the molecular density and to represent the Coulomb and exchange potentials accurately in each self-consistent field cycle.<sup>21</sup> All electrons were treated variationally (i.e., no frozen-core approximation). The electronic structures of  $Pd$ ,  $PdCl^-$ , and  $CH_3X$  were analyzed in terms of the quantitative molecular orbital model contained in Kohn–Sham DFT.<sup>25</sup> Recently, it has been shown that our approach is in good agreement with high-level ab initio calculations for oxidative addition reactions of the  $C-H$ ,<sup>8,11</sup>  $C-C$ ,<sup>12</sup>  $C-F$ ,<sup>13</sup> and  $C-Cl$ <sup>14</sup> bonds to palladium.

Equilibrium and transition state geometries were fully optimized using analytical gradient techniques. All structures were verified by frequency calculations: for minima, all normal modes have real frequencies, whereas transition states have one normal mode with an imaginary frequency. The character of the normal mode associated with the imaginary frequency was analyzed to ensure that the correct transition state was found.

Solvent effects in water have been estimated using the conductor-like screening model (COSMO),<sup>26</sup> as implemented in the ADF program.<sup>27</sup> The same parameters were used as described on page 49 of the Supporting Information of ref 28. This implies using a solvent-excluding surface with an effective radius for water of 1.9 Å, derived from the macroscopic density and molecular mass, and a relative dielectric constant of 78.4. The empirical parameter in the scaling function in the COSMO equation was chosen to be 0.0. The radii of the atoms were taken to be MM3 radii,<sup>29</sup> divided by 1.2, giving 1.350 Å for H, 1.700 Å for C, 1.425 Å for F, 1.725 Å for Cl, 1.850 Å for Br, 1.967 Å for I, 2.092 Å for At, and 1.975 Å for Pd. Using these radii gave differences of less than 3 kcal/mol between computed and experimental hydration energies of, for example, the chloride anion, tetramethylammonium cation, and tert-butyl cation.<sup>30</sup> Furthermore, the above computational settings were tested on the complexation energy of  $F^-$  and  $C_2H_5F$ . At ZORA-

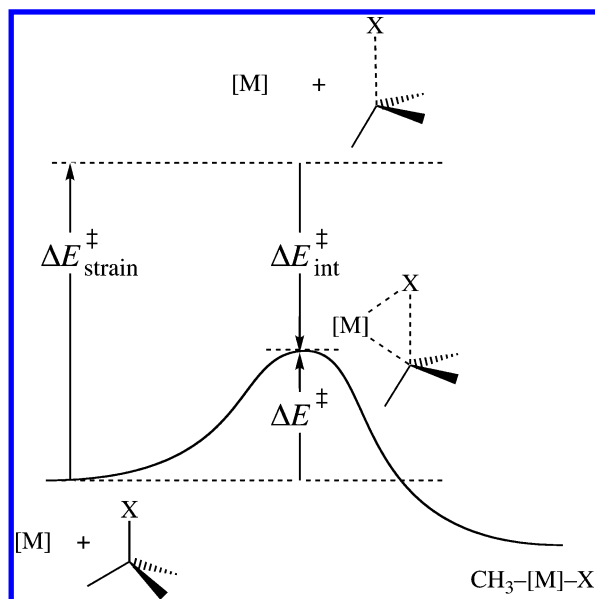


**Figure 1.** Illustration of the activation strain model in the case of oxidative insertion of a metal complex [M] into a C–X bond. The activation energy  $\Delta E^\ddagger$  is decomposed into the activation strain  $\Delta E^\ddagger_{\text{strain}}$  and the stabilizing TS interaction  $\Delta E^\ddagger_{\text{int}}$  between the reactants in the transition state.

BLYP/QZ4P, this is  $-19.0$  kcal/mol in the gas phase and a much smaller  $-0.2$  kcal/mol when solvent effects in water are included by COSMO. This is in complete agreement with previous observations.<sup>31</sup>

**2.2. Activation Strain Analyses.** To gain insight into how the use of different inserting metal complexes, namely, bare Pd and  $\text{PdCl}^-$ , and different substrates, namely,  $\text{CH}_3\text{X}$ , affects the activation barriers of the different oxidative addition reactions, the reactions were analyzed using the activation strain model of chemical reactivity.<sup>7,9,10,19</sup> In this model, the activation energy  $\Delta E^\ddagger$  is decomposed into the activation strain  $\Delta E^\ddagger_{\text{strain}}$  and the TS interaction  $\Delta E^\ddagger_{\text{int}}$  (see eq 2 and Figure 1):

$$\Delta E^\ddagger = \Delta E^\ddagger_{\text{strain}} + \Delta E^\ddagger_{\text{int}} \quad (2)$$

The activation strain  $\Delta E^\ddagger_{\text{strain}}$  is the strain energy associated with deforming the reactants from their equilibrium geometry to the geometry they acquire in the activated complex (Figure 1). The TS interaction  $\Delta E^\ddagger_{\text{int}}$  is the actual interaction energy between the deformed reactants in the transition state. In the present study, one of the reactants is either Pd or  $\text{PdCl}^-$ , and the other reactant is one of the substrates  $\text{CH}_3\text{X}$ .

**2.3. Ab Initio Calculations.** On the basis of the ZORA-BLYP/QZ4P optimized geometries, ab initio dissociation energies of the  $\text{CH}_3\text{--X}$  bonds were calculated at the advanced correlated CCSD(T) level<sup>32</sup> with the program package DIRAC.<sup>33</sup> A full all-electron four-component Dirac–Coulomb approach was used, which allowed nonrelativistic calculations with the Lévy–Leblond approximation,<sup>34</sup> relativistic calculations without spin–orbit coupling using a spin-free Dirac–Coulomb Hamiltonian,<sup>35</sup> and relativistic calculations using the unmodified Dirac–Coulomb Hamiltonian, which includes spin–orbit coupling [DC-CCSD(T)]. The two-electron integrals exclusively over the small components

have been neglected and corrected with a simple Coulombic correction, which has been shown to be reliable.<sup>36</sup> The basis sets used for hydrogen, carbon, fluorine, and chlorine were Dunning’s correlation consistent augmented triple- $\zeta$  (aug-cc-pVTZ) basis sets,<sup>37</sup> and for bromine, iodine, and astatine, Dyall’s relativistically optimized triple- $\zeta$  basis sets were used.<sup>38</sup>

### 3. Results and Discussion

**3.1. Reaction Profiles and Geometries.** In this section, we discuss the fully relativistic PESs in the gas phase of the various oxidative addition reactions as well as the geometries of the stationary points, that is, all computed at the ZORA-BLYP/QZ4P level. In the next section, we examine how relativity has affected the trends in reactivity. Thereafter, we examine how solvent effects in water affect these trends. Finally, we analyze these trends in the framework of the activation strain model. Structural results are summarized in Figure 2 and Table 1 (relativistically) and Table 2 (relativistically in water), and results about reaction profiles are given in Table 3 and in Figures 3 and 4. Structural results for the nonrelativistic calculations, energies with zero-point vibrational energy correction, and enthalpies at 298.15 K can be found in the Supporting Information.

The reactions of  $\text{Pd} + \text{CH}_3\text{F}$ ,  $\text{Pd} + \text{CH}_3\text{Cl}$ , and  $\text{PdCl}^- + \text{CH}_3\text{Cl}$  have been reported before.<sup>10,13,14</sup> It was shown that our computational method (ZORA with the BLYP functional) gives results that are in good agreement with high-level relativistic ab initio benchmark calculations. Here, we present a comprehensive overview of all reactions of Pd and  $\text{PdCl}^-$  with  $\text{CH}_3\text{X}$ .

All reactions proceed from the reactants via two distinct pathways, either via direct oxidative insertion ( $\text{OxIn}$ ) or via  $\text{S}_{\text{N}}2$  substitution, to the product, see Figure 2. For the  $\text{OxIn}$  pathway, the reaction proceeds from the reactants R via the formation of a stable reactant complex  $\text{RC}_{\text{OxIn}}$ , in which the halogen atom coordinates to the palladium atom, to a transition state  $\text{TS}_{\text{OxIn}}$  and, finally, a stable product P (Figure 2). There is one exception, namely, the addition of  $\text{CH}_3\text{F}$  to Pd. Here, the reaction proceeds from the same reactant complex as the alternative  $\text{S}_{\text{N}}2$  pathway, because the F–Pd coordination bond is too weak to produce a stable reactant complex (vide infra).

The  $\text{S}_{\text{N}}2$  pathway to oxidative addition proceeds via two consecutive stages: first, the actual nucleophilic substitution and followed by a rearrangement of the expelled leaving group toward palladium. The exact nature of this pathway and the shape of the reaction profile depend on the particular model reaction, that is, on the halogen atom in the C–X bond and on whether the metal experiences anion assistance ( $\text{PdCl}^-$ ) or not (Pd). For all neutral  $\text{Pd} + \text{CH}_3\text{X}$  and for  $\text{PdCl}^- + \text{CH}_3\text{F}$  and  $\text{CH}_3\text{Cl}$ , the  $\text{S}_{\text{N}}2$  reaction proceeds from the reactants via formation of a stable reactant complex,  $\text{RC}_{\text{S}_{\text{N}}2}$ , that differs from  $\text{RC}_{\text{OxIn}}$ . In the  $\text{S}_{\text{N}}2$  reactant complex  $\text{RC}_{\text{S}_{\text{N}}2}$ ,  $\text{CH}_3\text{X}$  coordinates either via one hydrogen atom in an  $\eta^1$  fashion or via two hydrogen atoms in an  $\eta^2$  fashion to Pd (see Figure 2), completely analogous to the reactant complexes found previously for the reactions of Pd with methane<sup>11</sup> and ethane.<sup>12</sup> The distinction between coordination

**Table 1.** Geometry Parameters<sup>a</sup> (in Å, Degrees) of Stationary Points on the Potential Energy Surface along the Reaction Coordinates of the OxIn and S<sub>N</sub>2-Type Pathways of Pd and PdCl<sup>−</sup> Addition to the C–X Bond of CH<sub>3</sub>X, with X = F, Cl, Br, I, and At, Computed Relativistically in the Gas Phase<sup>b</sup>

		Pd					PdCl <sup>−</sup>				
		F	Cl	Br	I	At	F	Cl	Br	I	At
R	C–X	1.413	1.818	1.986	2.189	2.295					
	∠H–C–H	108.5	108.1	107.3	107.1	106.6					
RC <sub>OxIn</sub>	C–X	1.411 <sup>c</sup>	1.853	2.030	2.226	2.336	1.423	1.901	2.112	2.298	2.422
	Pd–X	3.301 <sup>c</sup>	2.324	2.425	2.529	2.616	2.429	2.277	2.390	2.515	2.611
	Pd–C	2.372 <sup>c</sup>	3.516	3.669	3.817	3.909	3.133	3.582	3.850	4.037	4.228
	∠H–C–H	110.5 <sup>c</sup>	111.8	112.5	112.4	112.8	111.3	112.0	112.8	112.4	112.7
TS <sub>OxIn</sub>	C–X	1.786	2.046	2.194	2.379	2.477	1.733	2.152	2.327	2.491	2.587
	Pd–X	2.304	2.355	2.448	2.554	2.637	2.227	2.315	2.424	2.549	2.639
	Pd–C	2.111	2.506	2.643	2.730	2.807	2.462	2.790	2.902	2.916	2.978
	∠H–C–H	111.1	112.6	113.2	112.9	113.3	113.8	114.4	114.8	114.2	114.3
P	C–X	2.944	3.209	3.319	3.465	3.539	2.892	3.244	3.337	3.502	3.580
	Pd–X	1.938	2.250	2.381	2.543	2.632	2.020	2.352	2.492	2.658	2.751
	Pd–C	1.997	2.001	2.002	2.005	2.006	2.016	2.025	2.026	2.030	2.030
	∠H–C–H	112.5	112.4	112.3	112.1	112.0	111.9	111.9	111.9	111.9	111.8
RC <sub>S<sub>N</sub>2</sub>	C–X	1.411	1.824	2.004	2.222	2.390	1.447	1.899	<i>d</i>	<i>d</i>	<i>d</i>
	Pd–X	3.301	3.768	3.970	4.253	4.567	3.352	3.799	<i>d</i>	<i>d</i>	<i>d</i>
	Pd–C	2.372	2.383	2.366	2.352	2.313	2.308	2.280	<i>d</i>	<i>d</i>	<i>d</i>
	∠H–C–H	110.5	111.2	112.4	113.4	117.0	111.4	112.9	<i>d</i>	<i>d</i>	<i>d</i>
TS <sub>S<sub>N</sub>2</sub>	C–X	1.851 <sup>e</sup>	<i>d</i>	<i>d</i>	<i>d</i>	<i>d</i>	2.359	2.009	<i>d</i>	<i>d</i>	<i>d</i>
	Pd–X	2.806 <sup>e</sup>	<i>d</i>	<i>d</i>	<i>d</i>	<i>d</i>	3.843	3.976	<i>d</i>	<i>d</i>	<i>d</i>
	Pd–C	1.926 <sup>e</sup>	<i>d</i>	<i>d</i>	<i>d</i>	<i>d</i>	1.963	2.214	<i>d</i>	<i>d</i>	<i>d</i>
	∠H–C–H	114.7 <sup>e</sup>	<i>d</i>	<i>d</i>	<i>d</i>	<i>d</i>	112.2 <sup>f</sup>	117.6	<i>d</i>	<i>d</i>	<i>d</i>
IM <sub>S<sub>N</sub>2</sub>	C–X	3.575 <sup>e</sup>	<i>d</i>	<i>d</i>	<i>d</i>	<i>d</i>	2.856 <sup>e</sup>	2.724	2.911	3.173	3.232
	Pd–X	3.166 <sup>e</sup>	<i>d</i>	<i>d</i>	<i>d</i>	<i>d</i>	3.457 <sup>e</sup>	4.546	4.755	5.044	5.113
	Pd–C	1.859 <sup>e</sup>	<i>d</i>	<i>d</i>	<i>d</i>	<i>d</i>	1.884 <sup>e</sup>	1.998	2.002	2.007	2.011
	∠H–C–H	120.0 <sup>e</sup>	<i>d</i>	<i>d</i>	<i>d</i>	<i>d</i>	107.2 <sup>e</sup>	115.0	114.4	113.9	113.9
TS <sub>S<sub>N</sub>2-ra</sub>	C–X	2.566	3.192	3.425	3.641	3.742	2.604	3.354	3.570	3.876	3.981
	Pd–X	2.508	4.022	4.329	4.342	4.506	3.262	4.311	4.517	4.819	4.912
	Pd–C	2.019	2.018	2.020	2.007	2.009	1.969	1.997	2.001	2.005	2.007
	∠H–C–H	117.2	114.1	113.8	111.5	111.3	113.5	112.9	112.8	112.7	112.6

<sup>a</sup> See Figure 2; for ∠H–C–H, the average of the three possible ∠H–C–H angles is given. <sup>b</sup> At the ZORA–BLYP/QZ4P level of theory. <sup>c</sup> Same as RC<sub>S<sub>N</sub>2</sub>. <sup>d</sup> Stationary point does not exist. <sup>e</sup> “Anomalous” PdCH<sub>2</sub>···HF structure, see text. <sup>f</sup> C in methyl group pointing toward Pd.

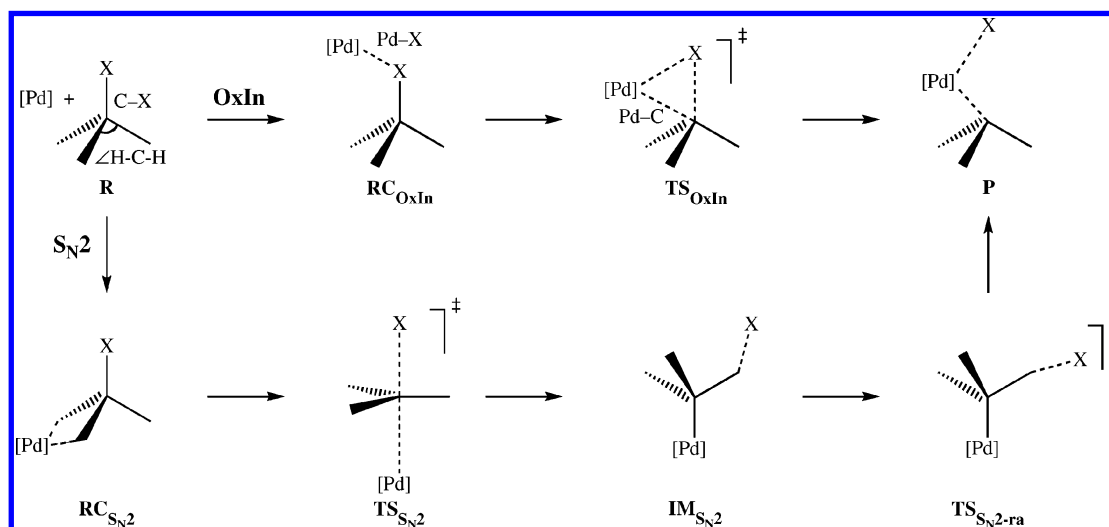


**Figure 2.** Structures of stationary points along the reaction coordinates of the OxIn- and S<sub>N</sub>2-type pathways for oxidative addition of the halomethane C–X bond to [Pd], with [Pd] = Pd and PdCl<sup>−</sup> and with X = F, Cl, Br, I, and At. See Tables 1–2 for values of selected geometry parameters, calculated at various levels of theory.



**Table 2.** Geometry Parameters<sup>a</sup> (in Å, Degrees) of Stationary Points on the Potential Energy Surface along the Reaction Coordinates of the OxIn and S<sub>N</sub>2-Type Pathways of Pd and PdCl<sup>−</sup> Addition to the C–X Bond of CH<sub>3</sub>X, with X = F, Cl, Br, I, and At, Computed Relativistically including Solvent Effects in Water<sup>b</sup>

		Pd					PdCl <sup>−</sup>				
		F	Cl	Br	I	At	F	Cl	Br	I	At
R	C–X	1.437	1.832	1.997	2.192	2.300					
	∠H–C–H	107.7	107.4	106.7	106.7	106.3					
RC <sub>OxIn</sub>	C–X	1.436 <sup>c</sup>	1.862	2.032	2.218	2.326	1.455	1.863	2.035	2.223	2.332
	Pd–X	3.266 <sup>c</sup>	2.312	2.416	2.525	2.611	2.288	2.320	2.428	2.548	2.637
	Pd–C	2.333 <sup>c</sup>	3.513	3.658	3.798	3.874	3.302	3.535	3.703	3.864	3.944
	∠H–C–H	111.2 <sup>c</sup>	112.3	112.9	112.6	113.0	112.0	112.2	112.8	112.5	112.9
TS <sub>OxIn</sub>	C–X	1.861	2.083	2.222	2.390	2.484	1.825	2.149	2.276	2.432	2.518
	Pd–X	2.592	2.327	2.430	2.544	2.626	2.157	2.327	2.442	2.570	2.656
	Pd–C	2.020	2.583	2.672	2.718	2.779	2.503	2.622	2.680	2.695	2.743
	∠H–C–H	109.5	113.7	113.9	113.3	113.5	115.3	114.3	114.2	113.5	113.5
P	C–X	2.949	3.203	3.309	3.444	3.517	2.928	3.243	3.320	3.466	3.571
	Pd–X	2.009	2.291	2.413	2.562	2.648	2.054	2.355	2.485	2.635	2.714
	Pd–C	1.993	1.999	2.000	2.004	2.005	2.022	2.031	2.033	2.038	2.037
	∠H–C–H	112.9	112.7	112.6	112.4	112.2	111.9	112.0	111.9	111.8	111.8
RC <sub>S<sub>N</sub>2</sub>	C–X	1.436	1.842	2.022	2.227	<i>d</i>	1.440	1.845	2.023	2.221	2.425
	Pd–X	3.266	3.724	3.921	4.201	<i>d</i>	3.265	3.687	3.856	4.084	4.453
	Pd–C	2.333	2.343	2.326	2.323	<i>d</i>	2.332	2.335	2.319	2.323	2.247
	∠H–C–H	111.2	111.8	113.0	113.7	<i>d</i>	111.2	111.6	112.6	112.7	118.4
TS <sub>S<sub>N</sub>2</sub>	C–X	1.838	2.162	2.266	2.447	<i>d</i>	1.927	2.173	2.267	2.504	2.557
	Pd–X	4.004	4.270	4.360	4.554	<i>d</i>	3.758	4.078	4.198	4.418	4.488
	Pd–C	2.165	2.185	2.196	2.195	<i>d</i>	2.044	2.124	2.152	2.135	2.152
	∠H–C–H	119.9	119.6	119.4	119.4	<i>d</i>	119.6 <sup>e</sup>	119.9	119.8	120.0	119.9
IM <sub>S<sub>N</sub>2</sub>	C–X	2.381	2.879	2.926	3.032	3.038	3.275	5.187	4.318	3.999	3.805
	Pd–X	4.398	4.891	4.946	5.063	5.078	4.132	6.961	6.052	5.976	5.782
	Pd–C	2.017	2.012	2.021	2.031	2.040	2.001	1.999	2.000	2.003	2.009
	∠H–C–H	116.4	115.7	115.9	116.0	116.3	113.1	112.8	112.7	112.8	112.9
TS <sub>S<sub>N</sub>2–ra</sub>	C–X	2.931	3.841	3.990	4.139	4.142	3.241	4.088	4.299	4.543	4.628
	Pd–X	4.611	4.845	5.001	5.138	5.147	4.073	4.775	5.034	5.294	5.329
	Pd–C	1.991	1.987	1.989	1.993	1.998	2.000	2.001	2.001	2.001	2.001
	∠H–C–H	114.3	114.7	114.6	114.3	114.0	113.1	112.8	112.8	112.7	112.7

<sup>a</sup> See Figure 2; for ∠H–C–H, the average of the three possible ∠H–C–H angles is given. <sup>b</sup> At the ZORA–BLYP/QZ4P level of theory, including solvent effects in water by COSMO. <sup>c</sup> Same as RC<sub>S<sub>N</sub>2</sub>. <sup>d</sup> Stationary point does not exist. <sup>e</sup> C in methyl group pointing toward Pd.

to one or two hydrogen atoms is not important from an energetical point of view. Thus, enforcing  $\eta^2$  coordination in the case of an  $\eta^1$  equilibrium structure (and vice versa) leads to a destabilization of not more than a few tenths of a kilocalorie per mole. From RC<sub>S<sub>N</sub>2</sub>, the S<sub>N</sub>2 substitution can then proceed via transition state TS<sub>S<sub>N</sub>2</sub> to intermediate IM<sub>S<sub>N</sub>2</sub> in which the C–X bond is broken. However, for the anion-assisted reactions of PdCl<sup>−</sup> + CH<sub>3</sub>Br, CH<sub>3</sub>I, and CH<sub>3</sub>At, the intermediate IM<sub>S<sub>N</sub>2</sub> is rather stable, and it is formed spontaneously, that is, via a barrierless substitution process lacking both a stable encounter complex RC<sub>S<sub>N</sub>2</sub> and a transition state TS<sub>S<sub>N</sub>2</sub>.

On the other hand, for the reactions of Pd + CH<sub>3</sub>Cl, CH<sub>3</sub>–Br, CH<sub>3</sub>I and CH<sub>3</sub>At, the expulsion of the leaving group goes with (energetically highly unfavorable) charge separation. This causes the intermediate structure IM<sub>S<sub>N</sub>2</sub>, i.e., PdCH<sub>3</sub><sup>+</sup>...X<sup>−</sup>, to become labile (i.e., it is no longer a local minimum) with respect to spontaneous back reaction to the reactant complex RC<sub>S<sub>N</sub>2</sub>. Consequently, the first and only transition state encountered along the S<sub>N</sub>2 pathway of Pd + CH<sub>3</sub>Cl, CH<sub>3</sub>–Br, CH<sub>3</sub>I and CH<sub>3</sub>At is TS<sub>S<sub>N</sub>2–ra</sub> which is associated with the rearrangement of the X<sup>−</sup> leaving group from carbon to palladium yielding the product P of oxidative addition.

There are some marked differences between the S<sub>N</sub>2 pathways for the addition of CH<sub>3</sub>F compared to that of the other substrates (for a detailed discussion, see ref 13). In the first place, the C–F bond is much stronger than the other C–X bonds (vide infra) and activation of the former is associated with significantly higher barriers (via both OxIn and S<sub>N</sub>2). Thus, at variance with the other substrates, the minimum energy path for Pd approaching CH<sub>3</sub>F from the backside is, in a sense, redirected from straight nucleophilic substitution and proceeds instead via a relatively low-energy transition state for insertion into a C–H bond (not shown here). Furthermore, the much higher basicity of F<sup>−</sup> compared to the other X<sup>−</sup> causes the former, after its expulsion in the actual S<sub>N</sub>2 transition state TS<sub>S<sub>N</sub>2</sub> and on its way toward Pd or PdCl<sup>−</sup>, to abstract a proton from the methyl moiety, under formation of an “anomalous” structure PdCH<sub>2</sub>...HF or [PdCl]CH<sub>2</sub><sup>−</sup>...HF for the intermediate complex IM<sub>S<sub>N</sub>2</sub> (i.e., not PdCH<sub>3</sub><sup>+</sup>...F<sup>−</sup> or [PdCl]CH<sub>3</sub>...X<sup>−</sup>). From this intermediate, fluoride migrates via the normal transition state TS<sub>S<sub>N</sub>2–ra</sub> toward Pd or PdCl<sup>−</sup> under formation of the product CH<sub>3</sub>–PdF or CH<sub>3</sub>[PdCl]F<sup>−</sup>.

Regarding the energetics of the reaction, the following trends can be observed. Along X = F, Cl, Br, I, and At, the

**Table 3.** Energies (in kcal/mol) Relative to Reactants of Stationary Points on the Potential Energy Surface along the Reaction Coordinates of the OxIn- and  $S_N2$ -Type Pathways of Pd and  $PdCl^-$  Addition to the C–X Bond of  $CH_3X$ , with X = F, Cl, Br, I, and At<sup>a</sup>

		RC <sub>OxIn</sub>	TS <sub>OxIn</sub>	P	RC <sub>S<sub>N2</sub></sub>	TS <sub>S<sub>N2</sub></sub>	IM <sub>S<sub>N2</sub></sub>	TS <sub>S<sub>N2</sub>-ra</sub>
Nonrelativistic in Gas Phase								
Pd	F	-3.0 <sup>b</sup>	23.2	-1.0	-3.0	39.6	31.5 <sup>c</sup>	38.8
	Cl	-7.8	5.4	-17.5	-2.7	<i>d</i>	<i>d</i>	31.4
	Br	-10.3	0.1	-22.0	-2.8	<i>d</i>	<i>d</i>	25.5
	I	-16.1	-6.3	-25.7	-3.0	<i>d</i>	<i>d</i>	23.7
	At	-18.4	-8.9	-27.4	-3.3	<i>d</i>	<i>d</i>	20.4
$PdCl^-$	F	-12.9 <sup>b</sup>	13.1	-29.4	-12.9	5.8	4.0	5.1
	Cl	-13.0	-3.3	-45.1	-14.4	-12.9	-14.9	-11.9
	Br	-16.7	-8.4	-48.7	<i>d</i>	<i>d</i>	-20.6	-17.2
	I	-23.8	-14.9	-51.1	<i>d</i>	<i>d</i>	-24.2	-20.8
	At	-26.2	-17.5	-51.9	<i>d</i>	<i>d</i>	-25.8	-22.2
Relativistic in Gas Phase								
Pd	F	-5.6 <sup>b</sup>	17.2	-16.7	-5.6	25.5	10.9 <sup>c</sup>	29.6
	Cl	-13.3	-0.8	-33.4	-5.3	<i>d</i>	<i>d</i>	22.9
	Br	-16.2	-5.7	-37.7	-5.7	<i>d</i>	<i>d</i>	16.6
	I	-22.4	-12.2	-41.5	-6.2	<i>d</i>	<i>d</i>	9.9
	At	-22.6	-13.3	-42.7	-7.2	<i>d</i>	<i>d</i>	5.8
$PdCl^-$	F	-2.4	9.7	-39.4	-16.0	-1.8	-8.3	-2.2
	Cl	-17.6	-6.9	-54.7	-17.7	-17.2	-21.2	-18.3
	Br	-21.1	-11.6	-57.8	<i>d</i>	<i>d</i>	-26.7	-23.4
	I	-27.5	-17.2	-59.9	<i>d</i>	<i>d</i>	-30.6	-27.0
	At	-27.7	-17.9	-59.5	<i>d</i>	<i>d</i>	-32.2	-28.1
Relativistic in Water								
Pd	F	-7.6 <sup>b</sup>	10.5	-27.5	-7.6	3.6	1.5	3.7
	Cl	-15.7	-2.9	-40.4	-7.3	-3.1	-8.2	-4.5
	Br	-18.7	-7.7	-43.4	-7.8	-6.2	-10.7	-5.7
	I	-25.4	-14.4	-45.7	-8.2	-7.5	-10.9	-3.6
	At	-25.8	-15.6	-46.3	<i>d</i>	<i>d</i>	-12.1	-3.2
$PdCl^-$	F	-7.2	11.0	-37.4	-11.4	-1.3	-10.9	-10.4
	Cl	-19.1	-3.5	-45.9	-10.8	-7.0	-20.4	-18.8
	Br	-21.1	-7.3	-47.0	-11.2	-9.0	-20.9	-19.6
	I	-26.0	-12.3	-46.1	-10.9	-10.4	-18.3	-16.5
	At	-25.7	-12.5	-45.6	-11.4	-11.3	-17.6	-15.6

<sup>a</sup> Nonrelativistic in Gas Phase: computed fully nonrelativistically at BLYP/QZ4P. Relativistic in Gas Phase: computed fully relativistically at ZORA–BLYP/QZ4P. Relativistic in Water: computed fully relativistically at ZORA–BLYP/QZ4P including solvent effects in water by COSMO. For a definition of stationary points, see Figure 2. <sup>b</sup> Same as RC<sub>S<sub>N2</sub></sub>. <sup>c</sup> “Anomalous”  $PdCH_2\cdots HF$  structure, see text. <sup>d</sup> Stationary point does not exist.

reactant complex for direct insertion, RC<sub>OxIn</sub>, becomes increasingly stable, from -13.3 kcal/mol for Pd + CH<sub>3</sub>Cl to -26.2 kcal/mol for Pd + CH<sub>3</sub>At and from -2.4 kcal/mol for  $PdCl^-$  + CH<sub>3</sub>F to -27.7 kcal/mol for  $PdCl^-$  + CH<sub>3</sub>At, see Table 3 and Figure 3, upper diagrams. In contrast, the relative energy of the reactant complex for the  $S_N2$  pathway, RC<sub>S<sub>N2</sub></sub>, does not change much when the halogen in the substrate is changed. This is clearly seen from Figure 3, middle diagrams. In all cases, the reactant complexes for addition to  $PdCl^-$  are more stable than for addition to Pd; see again Table 3 and Figure 3.

All reaction barriers become lower along X = F, Cl, Br, I, and At. For example, the relative energy of TS<sub>OxIn</sub> changes from 17.2 for Pd + CH<sub>3</sub>F to -13.3 kcal/mol for Pd + CH<sub>3</sub>-At. The relative ordering of barriers for the two pathways

does not change along X: for addition to Pd, the relative energy of TS<sub>OxIn</sub> lies below the relative energy of TS<sub>S<sub>N2</sub>-ra</sub> with a difference of, for example, 12.4 kcal/mol in the case of CH<sub>3</sub>F and 19.1 kcal/mol in the case of CH<sub>3</sub>At. In contrast, for addition to  $PdCl^-$  for all CH<sub>3</sub>X's, the relative energy of TS<sub>S<sub>N2</sub>-ra</sub> lies below the relative energy of TS<sub>OxIn</sub> with a difference of, for example, 11.9 kcal/mol in the case of CH<sub>3</sub>F and 10.2 kcal/mol in the case of CH<sub>3</sub>At, see Table 3 and Figure 4, middle diagrams. This change of selectivity, from OxIn as the preferred pathway for addition to Pd, to  $S_N2$  as the preferred pathway for addition to  $PdCl^-$  has been observed before for the addition of CH<sub>3</sub>Cl and can be well-understood within the activation strain model by the stronger, more stabilizing TS interaction  $\Delta E_{int}^{\ddagger}$  in the case of  $PdCl^-$ , caused by the raise of Pd-4d-derived orbitals in  $PdCl^-$ , which translates into more stabilizing donor–acceptor orbital interactions between the metal and the substrate, see for a discussion ref 10. It is interesting to note that this same effect extends over all CH<sub>3</sub>X additions.

The exothermicity of the reaction, that is, the relative energy of the product, becomes larger along X = F, Cl, Br, I, and At, although there is a certain saturation for the largest halogens. The reaction energy changes for addition to Pd, for example, from -16.7 kcal/mol for CH<sub>3</sub>F to -33.4 kcal/mol for CH<sub>3</sub>Cl to -37.7 kcal/mol for CH<sub>3</sub>Br to -41.5 kcal/mol for CH<sub>3</sub>I to -42.7 kcal/mol for CH<sub>3</sub>At. The addition to  $PdCl^-$  is in all cases more exothermic than that to Pd, see Table 3 and Figure 3, lower diagrams.

In the next sections, the effects of relativity and of changing the environment from the gas phase to water on these trends will be investigated. In the last section, an analysis of the trends in reactivity will be given.

**3.2. Relativistic Effects.** The use of a relativistic treatment is significant, but it does not change the relative order of reactivity of CH<sub>3</sub>X oxidative addition to Pd and  $PdCl^-$  along the series of halogens. The effects of relativity can be revealed by comparing the fully relativistic PESs discussed above with the corresponding fully nonrelativistic PESs derived from nonrelativistic energies and nonrelativistic geometries of stationary points. Here, we discuss the relative electronic energy PESs summarized in Table 3 and Figures 3 and 4. Note, however, that the PESs including zero-point vibrational energy corrections and those based on relative enthalpies give rise to the same trends and relativistic effects (see Tables S2 and S3 in the Supporting Information).

Relativity stabilizes the PES of all CH<sub>3</sub>X oxidative addition reactions to Pd and  $PdCl^-$ , as illustrated by Figures 3 (compare dotted and dashed lines) and 4 (compare upper and middle diagrams). Reaction barriers are stabilized by up to 14.6 kcal/mol (for TS<sub>S<sub>N2</sub>-ra</sub> in the case of CH<sub>3</sub>At addition to Pd), and reactions become more exothermic by up to 16 kcal/mol (for Pd + CH<sub>3</sub>Cl; see Table 3). The effect increases in most cases as one proceeds along the reaction coordinate (see Figure 3; compare the difference between the dotted and dashed lines for both the reactant complexes and the product). Thus, in the case of Pd + CH<sub>3</sub>Cl, for example, the RC<sub>OxIn</sub>, TS<sub>OxIn</sub>, and P are relativistically stabilized by -5.5, -6.2, and -15.9 kcal/mol (compare

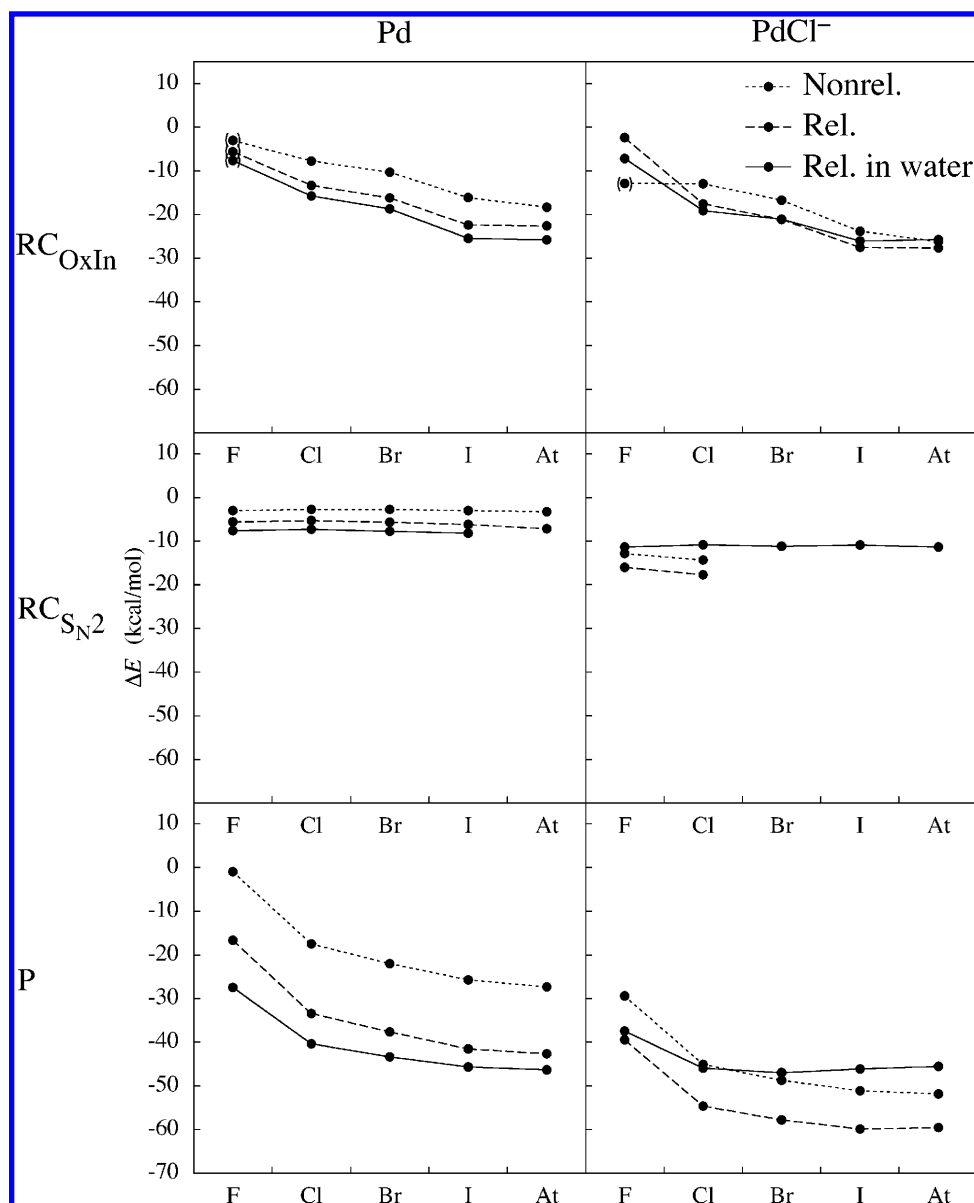


**Figure 3.** Relative energies (in kcal/mol) of the reactant complexes and the product for the OxIn- and  $S_N2$ -type pathways of Pd and  $PdCl^-$  addition to the C-X bond of  $CH_3X$ , with X = F, Cl, Br, I, and At. Dotted lines: calculated nonrelativistically in the gas phase. Dashed lines: calculated relativistically in the gas phase. Solid lines: calculated relativistically in water.

relativistic with nonrelativistic data in Table 3). One seemingly exceptional case is  $RC_{OxIn}$  for the  $CH_3F$  addition to  $PdCl^-$ , which seems to become more stable when relativity is turned off, see Figure 3, upper left diagram. But, in fact, the nonrelativistic  $RC_{OxIn}$  is very unstable, such that it does not even exist and changes into the more stable  $RC_{SN2}$ . One might expect relativistic effects to be more pronounced for the reactions involving the heavier halogens. This expectation is born out of the observation that relativistic effects on the  $CH_3-X$  bond strengths increase substantially along X = F, Cl, Br, I, and At (vide infra; see also Table 4). Interestingly, however, the relativistic stabilization of the stationary points becomes overall smaller, not stronger, along this series in X, with only two exceptions, namely,  $RC_{SN2}$  and  $TS_{SN2-ra}$ , for addition to Pd (see Table 3).

The relativistic effects originating from the halogen atoms obviously counteract and partially cancel those originating

from palladium. Closer inspection of the influence of relativity on the orbital energy levels shows what causes this. The only observable effect in the valence and subvalence orbitals, both on Pd as on the larger halogens, is the relativistic stabilization of the s orbitals. In the case of Pd, the stabilization of the empty 5s orbital (from  $-3.0$  to  $-3.4$  eV) increases its electron-accepting ability. This enhances the Pd-substrate interaction and is thus responsible for the relativistic stabilization of stationary points along the reaction coordinate. In the case of the halogens, the increasing stabilization of the filled valence *ns* orbital along the series of halogens (e.g., for F from  $-30.4$  to  $-30.5$  eV, for Br from  $-19.7$  to  $-20.4$  eV, and for At from  $-15.1$  to  $-19.4$  eV; not shown in diagrams or tables) causes the electron-donating ability to decrease. Thus, the relativistic effects stemming from the halogen atoms have a weakening effect on the Pd-substrate interaction which counteracts (but only

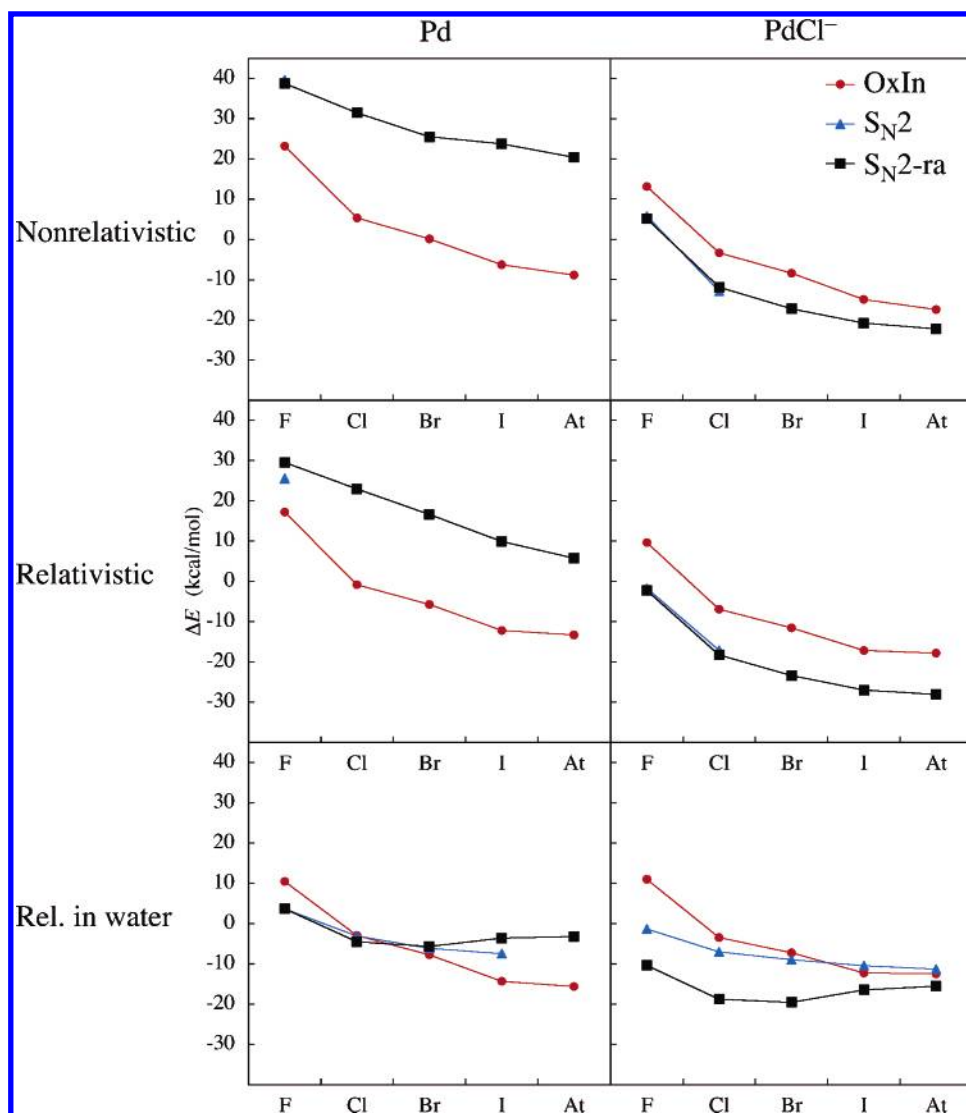


**Figure 4.** Reaction barriers relative to reactants (in kcal/mol) of the OxIn- and  $\text{S}_{\text{N}}2$ -type pathways of Pd and  $\text{PdCl}^-$  addition to the C–X bond of  $\text{CH}_3\text{X}$ , with X = F, Cl, Br, I, and At, calculated at different levels of theory.

partially cancels) the stabilizing relativistic effect originating from palladium.

Relativity also affects the geometries of all species involved in the oxidative addition reactions. The most striking and general effect is a shortening of the Pd–X bond distance (compare Table 2 and Table S1 in the Supporting Information). In a previous study, on the oxidative addition of HX and  $\text{X}_2$  to Pd, it was shown that geometry-relaxation processes caused by relativity are typically on the order of 1 kcal/mol or less and, thus, hardly affect the PES along the reaction coordinate.<sup>39</sup> The relativistic stabilization of stationary points along the reaction coordinate can be really directly attributed to the strengthening of the Pd–substrate interaction mentioned above.

**3.3. Solvent Effects.** Solvent effects, at variance with relativistic effects (vide supra), profoundly affect and qualitatively modify the characteristics of the reactions, in certain instances, to the extent that they change the preference from one to another pathway (see Table 3). Solvent effects are also markedly different for the neutral ( $\text{Pd} + \text{CH}_3\text{X}$ ) as compared to the anion-assisted model reactions ( $\text{PdCl}^- + \text{CH}_3\text{X}$ ). In the former, solvation stabilizes all stationary points

along the reaction coordinate relative to the reactants. Thus, in water, the reactant complexes of  $\text{Pd} + \text{CH}_3\text{X}$  become more strongly bound, activation barriers are reduced, and the reaction becomes more exothermic. This becomes clear, for example, by comparing solid lines (water) with dashed lines (gas phase) in Figure 3. The stabilization relative to reactants that is caused by solvation can be easily understood from electrostatic arguments. The interaction of neutral Pd with neutral  $\text{CH}_3\text{X}$  induces a charge separation  $\text{Pd}^{\delta+} \cdots \text{CH}_3\text{X}^{\delta-}$  which is stabilized by the concomitant polarization of the solvent medium. Likewise, the ionic intermediate structure  $\text{PdCH}_3^+ \cdots \text{X}^-$  ( $\text{IM}_{\text{S}_{\text{N}}2}$ ) which is labile in the gas phase (or, in the case of  $\text{Pd} + \text{CH}_3\text{F}$ , exists as  $\text{PdCH}_2 \cdots \text{HF}$ , vide supra) is particularly stabilized and reappears as a stable intermediate in water (see Table 3).

On the other hand, solvation of the anion-assisted model reactions ( $\text{PdCl}^- + \text{CH}_3\text{X}$ ) leads in many (but not all) cases to a *destabilization* of stationary points along the reaction coordinate (see Table 3 and Figures 3 and 4). The reason is mainly the strong stabilization of the reactant  $\text{PdCl}^-$  in which the excess negative charge is highly localized, leading to a strongly stabilizing electrostatic (and orbital) interaction with



**Table 4.** Homolytic and Heterolytic Dissociation Energies (in kcal/mol) of the CH<sub>3</sub>–X Bond for X = F, Cl, Br, I, and At, Computed at Various Levels of DFT and ab Initio Theory<sup>a</sup>

method	F	Cl	Br	I	At
Homolytic					
BLYP//BLYP <sup>b</sup>	114.7	82.9	72.1	62.1	57.5
BLYP	114.7	82.9	72.1	62.1	57.5
ZORA-BLYP	114.6	82.7	71.7	61.3	55.9
SO-ZORA-BLYP	114.6	82.4	68.3	54.3	41.0
SO-ZORA-BLYP in water <sup>c</sup>	117.9	84.2	70.7	56.1	42.5
CCSD(T)	111.1	83.0	72.6	63.2	58.9
SFDC-CCSD(T)	111.1	82.9	72.2	62.2	56.6
DC-CCSD(T)	110.7	82.0	68.8	55.7	41.7
experiment <sup>d</sup>	109.8	83.8	69.8	56.9	
Heterolytic					
ZORA-BLYP	262.1	227.5	220.7	214.7	213.5
ZORA-BLYP in water <sup>c</sup>	80.5	72.2	71.7	74.9	75.8

<sup>a</sup> Geometries optimized at ZORA-BLYP/QZ4P, unless stated otherwise. BLYP = nonrelativistic BLYP/QZ4P. ZORA-BLYP = scalar ZORA-relativistic BLYP/QZ4P. SO-ZORA-BLYP = spin-orbit ZORA-relativistic BLYP/QZ4P. CCSD(T) = nonrelativistic CCSD(T). SFDC-CCSD(T) = CCSD(T) with relativistic spin-free Dirac-Coulomb Hamiltonian excluding spin-orbit coupling. DC-CCSD(T) = CCSD(T) with relativistic unmodified Dirac-Coulomb Hamiltonian including spin-orbit coupling. All CCSD(T) values at all levels of theory have been corrected for the basis-set superposition error. <sup>b</sup> Geometries optimized nonrelativistically at BLYP/QZ4P. <sup>c</sup> Solvent effects in water by COSMO; see text. <sup>d</sup> Obtained from corresponding enthalpies of formation at 298 K from ref 41.

the solvent.<sup>31</sup> In the other stationary points (i.e., RC, TS, etc.), the negative charge is delocalized, because of the PdCl<sup>−</sup>/substrate interaction, over a larger area, leading to a less favorable electrostatic (and orbital) interaction.<sup>31</sup> Note however that the reactant complex structure PdCl<sup>−</sup>⋯CH<sub>3</sub>X (RC<sub>S<sub>N</sub>2</sub>), which is labile and thus absent in the gas phase, is stabilized more than TS<sub>S<sub>N</sub>2</sub> and reappears as a stable species in water (see Table 3 and Figure 4). For RC<sub>S<sub>N</sub>2</sub> and P, the relative energy clearly becomes less negative. For example, in the case of PdCl<sup>−</sup> + CH<sub>3</sub>Cl, it changes from −17.7 to −10.8 kcal/mol and from −54.7 to −45.9 kcal/mol, respectively (see Table 3 and Figure 3). For RC<sub>OxIn</sub>, the effect is somewhat less clear-cut. What is clear, however, is the absence of a pronounced and general stabilization of transition states, at variance with the neutral Pd + CH<sub>3</sub>X reactions (see Figure 4).

The most striking phenomenon associated with solvation is, however, the change in preference from one to another pathway. Interestingly, the occurrence of this solvation-induced change in reaction mechanism depends on which C–X bond is activated and also on whether anion assistance is present (PdCl<sup>−</sup>) or not (Pd). The neutral reactions of Pd + CH<sub>3</sub>X shift because of solvation from OxIn (preferred in the gas phase) to S<sub>N</sub>2, but this shift occurs only for the smaller halogens, F and Cl (see Figure 4). On the other hand, the anion-assisted reactions of PdCl<sup>−</sup> + CH<sub>3</sub>X shift from S<sub>N</sub>2 (preferred in the gas phase) to OxIn, but this time, the shift happens only for the heavier halogens, I and At (see Figure 4). For example, for Pd + CH<sub>3</sub>F, the barrier for the OxIn pathway is lowered by solvation from 17.2 to 10.5 kcal/mol, but the barrier for the S<sub>N</sub>2 pathway is lowered much

more, from 29.6 to 3.7 kcal/mol (see Table 3). On the other hand, for Pd + CH<sub>3</sub>At, the barrier for the OxIn pathway is lowered by solvation from −13.3 to −15.6 kcal/mol, and the barrier for the S<sub>N</sub>2 pathway is lowered more, from 5.8 to −3.2 kcal/mol, but not nearly enough to make the S<sub>N</sub>2 pathway the preferred pathway (see Table 3). For comparison, the S<sub>N</sub>2 barrier of PdCl<sup>−</sup> + CH<sub>3</sub>At, which is absent in the gas phase, is in water about 1 kcal/mol higher than the corresponding OxIn barrier (see Table 3 and Figure 4). Furthermore, the S<sub>N</sub>2-ra barrier of PdCl<sup>−</sup> + CH<sub>3</sub>At in water is only slightly, that is, 3 kcal/mol, lower than the OxIn barrier, whereas it is more than 10 kcal/mol lower than the OxIn barrier in the gas phase.

Solvation apparently stabilizes the S<sub>N</sub>2 transition states of the lighter C–X bonds significantly more efficiently than the corresponding OxIn transition states but also more than the S<sub>N</sub>2 transition states of the heavier C–X bonds (see Table 3 and Figure 4). Note that this biased solvation stabilization even breaks the intrinsic (i.e., gas-phase) trend of continuously decreasing S<sub>N</sub>2-ra reaction barriers along the halogens: thus, in water, the S<sub>N</sub>2-ra barrier still decreases from F to Cl to Br, but thereafter, it increases from Br to I to At (see Figure 4).

### 3.4. Activation Strain Analysis of Gas-Phase Reactivity.

In the following, we aim at understanding the origin of the above trends in reactivity; that is, we wish to understand how the feasibility of reaction mechanisms is exactly determined by the nature of the C–X bond, anion assistance, and solvent effects. We do this using the activation strain model, which, as pointed out earlier, is a fragment approach to understanding activation barriers in terms of properties of the reactants, here, the catalyst [Pd] and the substrate CH<sub>3</sub>X. Thus, the activation energy  $\Delta E^\ddagger$  is decomposed into the activation strain  $\Delta E_{\text{strain}}^\ddagger$  associated with deforming the reactants from their equilibrium structures to the geometries they adopt in the TS plus the TS interaction  $\Delta E_{\text{int}}^\ddagger$ , that is, the interaction between the deformed reactants (see eq 2).

First, we explore and analyze the metal–substrate bonding in the reactant complexes and the C–X bond strength in the halomethane substrates. This facilitates interpreting the activation strain analyses of activation barriers  $\Delta E^\ddagger$ , as the latter are the result of an interplay between these two quantities which appear as the metal–substrate TS interaction  $\Delta E_{\text{int}}^\ddagger$  and the activation strain  $\Delta E_{\text{strain}}^\ddagger$  that mainly stems from C–X bond elongation. The metal–substrate interaction between the reactants is provided, among others, by the donor–acceptor orbital interactions between the Pd 4d orbitals (or the Pd 4d-derived orbitals in PdCl<sup>−</sup>) and the substrate  $\sigma^*_{\text{C-X}}$  LUMO. These orbital interactions are strengthened by relativistic effects because, as is well-known, the latter destabilize the Pd 4d orbitals, which leads to a smaller, more favorable HOMO–LUMO gap between Pd and the substrate (the effect is further reinforced by relativistic stabilization of the Pd 5s acceptor orbital).<sup>7</sup> The relativistic strengthening of the metal–substrate interaction in the reactant complexes can be clearly recognized in Figure 3, in which nonrelativistic and relativistic gas-phase bond energies are connected by dotted and dashed lines, respectively.

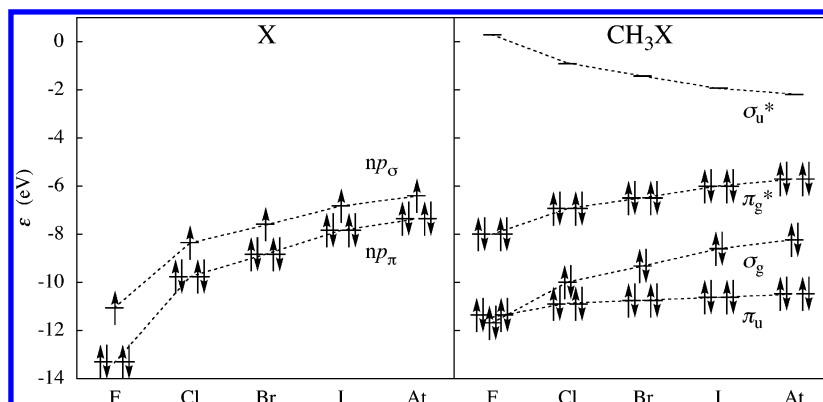


**Figure 5.** Kohn–Sham orbital energies  $\epsilon$  (in eV) of the frontier orbitals of X and  $\text{CH}_3\text{X}$  with X = F, Cl, Br, I, and At, at ZORA-BLYP/QZ4P.

The trend of increasing metal–substrate interaction in  $\text{RC}_{\text{OxIn}}$  along X = F, Cl, Br, I, and At (see Figure 3) can be easily understood on the basis of how the electronic structure of the substrate  $\text{CH}_3\text{X}$  depends on the halogen X (see Figure 5). The frontier orbitals of  $\text{CH}_3\text{X}$  are the degenerate  $\pi_g^*$  lone-pair HOMOs, which are mainly the halogen  $np_\pi$  atomic orbitals (AOs), and the  $\sigma_{\text{C-X}}^*$  LUMO, which is mainly the carbon 2s–halogen  $np_\sigma$  antibonding combination. Along X = F, Cl, Br, I, and At, the halogen  $np_\pi$  AOs rise in energy (the halogen becomes less electronegative) and become more diffuse. Thus, the halogen  $\pi_g^*$  lone-pair HOMOs in the substrate also increases in energy (because the halogen  $np_\pi$  AOs rise) while the antibonding  $\sigma_{\text{C-X}}^*$  LUMO decreases as the  $\langle 2s | np_\sigma \rangle$  overlap becomes smaller (because the halogen  $np_\sigma$  AO becomes more diffuse; see Figure 5). This reduces the HOMO–LUMO gaps for donation (substrate  $\pi_g^*$  lone-pair to metal 5s) and backdonation (metal 4d to substrate  $\sigma_{\text{C-X}}^*$ ) between Pd or  $\text{PdCl}^-$  and  $\text{CH}_3\text{X}$  and thus strengthens the interaction energy along this series (see Figure 3).

In  $\text{RC}_{\text{SN}2}$ , on the other hand, the metal–substrate interaction depends much less on the halogen atom X in the substrate  $\text{CH}_3\text{X}$  (in Figure 3, it seems to be essentially constant). The reason is that in  $\text{RC}_{\text{SN}2}$  the metal interacts predominantly through an agostic interaction with C–H bonds of the methyl group in  $\text{CH}_3\text{X}$  and therefore depends much less on X (for a more detailed discussion, see ref 18).

Next, we examine the other player, besides metal–substrate interaction, in the activation strain model, namely, the geometrical rigidity of the reactants. The latter shows up as the activation strain  $\Delta E_{\text{strain}}^\ddagger$ . It is predominantly determined by the C–X bond stretching in the TS and, thus, by the  $\text{CH}_3\text{--X}$  bond strengths  $D_{\text{C-X}}$  in the halomethane substrates. Thus, we have computed  $D_{\text{C-X}}$  associated with the reactions  $\text{CH}_3\text{--X} \rightarrow \text{CH}_3^\bullet + \text{X}^\bullet$  at BLYP/QZ4P (see Table 4). The bond strength  $D_{\text{C-X}}$  decreases continuously along X = F, Cl, Br, I, and At, from 114.6 (X = F) to 41.0 kcal/mol (X = At), at the spin–orbit corrected relativistic SO-ZORA-BLYP/QZ4P level of theory. This trend is mainly caused by the decreasing charge-stabilization that goes with the decreasing electronegativity difference across the  $\text{CH}_3\text{--X}$  bond when the halogen atom becomes less and less electronegative along the series.<sup>40</sup>

Before continuing the discussion of the interplay between metal–substrate interaction and geometrical deformation or

strain energy in the activation strain model, we briefly evaluate the performance of our approach for computing C–X bond strength (see also Table 4). To this end, we have carried out an accurate benchmark study at the CCSD(T) level of ab initio theory in combination with a Gaussian triple- $\zeta$  basis set. Relativistic effects have been assessed for both BLYP and CCSD(T), by carrying out the computations nonrelativistically [BLYP or CCSD(T)], scalar relativistically, that is, without spin–orbit coupling [ZORA-BLYP, spin-free Dirac-Coulomb, or SFDC-CCSD(T)], and relativistically including spin–orbit coupling [SO-ZORA-BLYP, Dirac-Coulomb, or DC-CCSD(T)] (see Section 2.3 for methodological details). The BLYP values agree well with those of the CCSD(T) benchmark, and they do so at each level of treating relativistic effects. For example,  $D_{\text{C-At}}$  amounts to 57.5, 55.9, and 41.0 kcal/mol at BLYP, ZORA-BLYP, and SO-ZORA-BLYP, which agrees within 1.4 kcal/mol with the 58.9, 56.6, and 41.7 kcal/mol obtained at CCSD(T), SFDC-CCSD(T), and DC-CCSD(T), respectively, including corrections for the basis-set superposition error (see Table 4). The DC-CCSD(T) benchmark in turn agrees within a few kilocalories per mole with experimental data<sup>41</sup> where available. Note that relativistic effects on the homolytic  $D_{\text{C-X}}$  are predominantly caused by spin–orbit coupling. The spin–orbit term stems from the species that have a doublet open-shell configuration, that is, the dissociation products  $\text{CH}_3^\bullet$  and especially  $\text{X}^\bullet$ . This is in line with earlier work by Ziegler and co-workers.<sup>40</sup> Spin–orbit coupling is a minor term for all closed-shell systems studied, that is, Pd,  $\text{PdCl}^-$ ,  $\text{CH}_3\text{X}$ , and the species at the stationary points along the PES of our model reactions.<sup>42</sup> Thus, whereas the computation of reliable homolytic bond dissociation energies requires consideration of spin–orbit effects, the relative energies of stationary points along the PESs of our model reactions (all closed-shell!) can be sufficiently accurately determined through a scalar relativistic approach (i.e., the ZORA-BLYP approach which is used throughout the present work).

Interestingly, the activation strain analyses, to which we now return, reveal that the trend in activation energies  $\Delta E^\ddagger$  of our gas-phase model reactions is mainly determined by the trend in C–X bond strength. The results of the analyses are listed in Table 5, both for the gas-phase and the condensed-phase model reactions which are discussed in this

**Table 5.** Analysis of the Reaction Barriers of the OxIn- and S<sub>N</sub>2-Type Pathways of Pd and PdCl<sup>−</sup> Addition to the C–X Bond of CH<sub>3</sub>X, with X = F, Cl, Br, I, and At, in Terms of the Activation Strain Model<sup>a</sup>

		Pd					PdCl <sup>−b</sup>				
		F	Cl	Br	I	At	F	Cl	Br	I	At
Relativistic in Gas Phase											
TS <sub>OxIn</sub>	$\Delta E^\ddagger$	17.2	−0.8	−5.7	−12.2	−13.3	9.7	−6.9	−11.6	−17.2	−17.9
	$\Delta E^\ddagger_{\text{strain}}$	37.0	10.0	7.2	5.4	4.6	22.2	14.1	12.5	9.4	8.3
	$\Delta E^\ddagger_{\text{int}}$	−19.8	−10.8	−12.9	−17.7	−17.9	−12.5	−21.0	−24.1	−26.6	−26.1
TS <sub>S<sub>N</sub>2</sub>	$\Delta E^\ddagger$	25.5	<i>c</i>	<i>c</i>	<i>c</i>	<i>c</i>	−1.8	−17.2	<i>c</i>	<i>c</i>	<i>c</i>
	$\Delta E^\ddagger_{\text{strain}}$	103.2	<i>c</i>	<i>c</i>	<i>c</i>	<i>c</i>	84.5	9.1	<i>c</i>	<i>c</i>	<i>c</i>
	$\Delta E^\ddagger_{\text{int}}$	−77.7	<i>c</i>	<i>c</i>	<i>c</i>	<i>c</i>	−86.2	−26.3	<i>c</i>	<i>c</i>	<i>c</i>
TS <sub>S<sub>N</sub>2−ra</sub>	$\Delta E^\ddagger$	29.6	22.9	16.6	9.9	5.8	−2.2	−18.3	−23.4	−27.0	−28.1
	$\Delta E^\ddagger_{\text{strain}}$	95.8	82.8	76.4	67.4	62.3	98.1	85.3	78.5	72.5	68.8
	$\Delta E^\ddagger_{\text{int}}$	−66.2	−59.8	−59.8	−57.6	−56.5	−100.3	−103.6	−101.8	−99.5	−96.9
Relativistic in Water											
TS <sub>OxIn</sub>	$\Delta E^\ddagger(\text{aq})$	10.5	−2.9	−7.7	−14.4	−15.6	11.0	−3.5	−7.3	−12.3	−12.5
	$\Delta E^\ddagger_{\text{strain}}(\text{aq})$	47.9	10.0	7.5	5.7	4.8	23.2	13.0	10.0	7.8	6.6
	$\Delta E^\ddagger_{\text{strain,pure}}$	53.4	11.4	8.3	5.9	5.0	28.9	14.9	11.2	8.2	6.9
	$\Delta E^\ddagger_{\text{strain,cav}}$	0.0	0.0	0.0	0.0	0.0	0.0	0.0	0.0	0.0	0.0
	$\Delta E^\ddagger_{\text{strain,solv}}$	−5.5	−1.4	−0.8	−0.2	−0.2	−5.7	−1.9	−1.2	−0.4	−0.3
	$\Delta E^\ddagger_{\text{int}}(\text{aq})$	−37.4	−12.9	−15.2	−20.1	−20.5	−12.1	−16.5	−17.3	−20.0	−19.1
	$\Delta E^\ddagger_{\text{int,desolv}}$	0.6	0.2	0.0	−0.3	−0.2	2.2	1.3	1.2	0.9	0.9
	$\Delta E^\ddagger_{\text{int,cav}}$	−1.5	−1.5	−1.5	−1.5	−1.5	−1.5	−1.5	−1.5	−1.5	−1.5
	$\Delta E^\ddagger_{\text{int,pure}}$	−36.5	−11.6	−13.8	−18.3	−18.8	−12.8	−16.4	−17.0	−19.5	−18.6
	( $\Delta E^\ddagger_{\text{int,gas}}$ )	(−33.7)	(−12.1)	(−14.0)	(−18.2)	(−18.3)	(−19.5)	(−22.5)	(−23.2)	(−25.9)	(−25.2)
TS <sub>S<sub>N</sub>2</sub>	$\Delta E^\ddagger(\text{aq})$	3.6	−3.1	−6.2	−7.5	<i>c</i>	−1.3	−7.0	−9.0	−10.4	−11.3
	$\Delta E^\ddagger_{\text{strain}}(\text{aq})$	23.4	13.9	10.2	9.0	<i>c</i>	35.6	18.2	13.1	14.3	11.5
	$\Delta E^\ddagger_{\text{strain,pure}}$	30.0	16.3	11.5	9.6	<i>c</i>	43.1	20.7	14.6	15.1	12.0
	$\Delta E^\ddagger_{\text{strain,cav}}$	0.0	0.0	0.0	0.0	<i>c</i>	0.0	0.0	0.0	0.0	0.0
	$\Delta E^\ddagger_{\text{strain,solv}}$	−6.6	−2.4	−1.3	−0.6	<i>c</i>	−7.5	−2.5	−1.5	−0.8	−0.5
	$\Delta E^\ddagger_{\text{int}}(\text{aq})$	−19.8	−16.9	−16.3	−16.5	<i>c</i>	−36.9	−25.2	−22.1	−24.7	−22.8
	$\Delta E^\ddagger_{\text{int,desolv}}$	1.8	1.0	0.7	0.4	<i>c</i>	2.8	2.1	1.8	1.6	1.4
	$\Delta E^\ddagger_{\text{int,cav}}$	−1.4	−1.4	−1.4	−1.4	<i>c</i>	−1.5	−1.5	−1.5	−1.5	−1.5
	$\Delta E^\ddagger_{\text{int,pure}}$	−20.1	−16.5	−15.6	−15.5	<i>c</i>	−38.2	−25.8	−22.5	−24.9	−22.8
	( $\Delta E^\ddagger_{\text{int,gas}}$ )	(−13.2)	(−12.9)	(−13.1)	(−13.9)	<i>c</i>	(−49.9)	(−38.8)	(−36.0)	(−39.3)	(−37.4)
TS <sub>S<sub>N</sub>2−ra</sub>	$\Delta E^\ddagger(\text{aq})$	3.7	−4.5	−5.7	−3.6	−3.2	−10.4	−18.8	−19.6	−16.5	−15.6
	$\Delta E^\ddagger_{\text{strain}}(\text{aq})$	80.6	75.5	71.7	69.4	66.6	88.6	81.0	77.0	74.0	71.1
	$\Delta E^\ddagger_{\text{strain,pure}}$	100.4	86.2	74.8	64.9	59.8	112.9	87.0	76.3	65.9	60.5
	$\Delta E^\ddagger_{\text{strain,cav}}$	0.1	0.1	0.1	0.1	0.1	0.1	0.1	0.1	0.1	0.1
	$\Delta E^\ddagger_{\text{strain,solv}}$	−19.9	−10.8	−3.2	4.4	6.7	−24.4	−6.1	0.6	8.0	10.5
	$\Delta E^\ddagger_{\text{int}}(\text{aq})$	−76.9	−79.9	−77.4	−72.9	−69.9	−99.1	−99.8	−96.5	−90.4	−86.6
	$\Delta E^\ddagger_{\text{int,desolv}}$	8.0	10.2	7.5	4.1	2.6	13.1	12.4	9.5	5.1	3.7
	$\Delta E^\ddagger_{\text{int,cav}}$	−1.4	−1.5	−1.4	−1.4	−1.5	−1.5	−1.5	−1.5	−1.5	−1.5
	$\Delta E^\ddagger_{\text{int,pure}}$	−83.5	−88.7	−83.4	−75.6	−71.0	−110.8	−110.8	−104.5	−94.0	−88.8
	( $\Delta E^\ddagger_{\text{int,gas}}$ )	(−57.0)	(−59.7)	(−55.9)	(−53.5)	(−52.0)	(−107.2)	(−102.4)	(−97.2)	(−91.1)	(−87.1)

<sup>a</sup> See footnote a of Table 3. <sup>b</sup> Activation strain values include strain in PdCl<sup>−</sup> species, which is nowhere larger than 0.6 kcal/mol, but mostly around 0.1 kcal/mol. <sup>c</sup> TS does not exist.

section and the following one, respectively (for the results of a *nonrelativistic* activation strain analysis, see Table S4 in the Supporting Information). The trend of a decreasing activation energy along X = F, Cl, Br, I, and At derives predominantly from the activation strain  $\Delta E^\ddagger_{\text{strain}}$  and despite a (in most but not all cases) counteracting trend in the metal–substrate TS interaction  $\Delta E^\ddagger_{\text{int}}$  (see Table 5, relativistic in gas phase). The activation strain  $\Delta E^\ddagger_{\text{strain}}$  decreases along X = F, Cl, Br, I, and At for all reaction steps and pathways (i.e., OxIn versus S<sub>N</sub>2 and S<sub>N</sub>2-ra) of the Pd- and PdCl<sup>−</sup>-induced reactions. For example, in the case of the

OxIn reactions of Pd + CH<sub>3</sub>X,  $\Delta E^\ddagger_{\text{strain}}$  decreases from 37.0 to 10.0 to 7.2 to 5.4 to 4.6 kcal/mol (see Table 5). Similar trends exist for the other model reactions with somewhat lower  $\Delta E^\ddagger_{\text{strain}}$  values for the PdCl<sup>−</sup>-induced OxIn reactions (with more eductlike and thus less deformed TSs, vide infra) and higher  $\Delta E^\ddagger_{\text{strain}}$  values for the S<sub>N</sub>2-type reactions (which feature TSs in which the substrate CH<sub>3</sub>X is significantly more deformed, vide infra). This trend of decreasing activation strain along X = F, Cl, Br, I, and At and, thus, the trend in activation energies  $\Delta E^\ddagger$  is directly inherited from the behavior of the C–X bond strength, which, as discussed

above, also weakens along this series in X. In this context, we note that the activation strain of the Pd-induced reactions arises exclusively from the substrate, in particular, the C–X elongation along the reaction coordinate. That of the PdCl<sup>−</sup>-induced reactions arises *almost* exclusively from the substrate: the PdCl<sup>−</sup> complex never contributes more than a few tenths of a kilocalorie per mole (not shown in Table 5).

Here, we wish to address two phenomena in more detail: (i) the increase in activation energy from OxIn to S<sub>N</sub>2 pathways and (ii) the much stronger decrease in activation energies due to anion assistance (i.e., if one goes from Pd to PdCl<sup>−</sup>) for the S<sub>N</sub>2 reactions than that for the OxIn reactions, which causes the preferred pathway to shift from OxIn for Pd + CH<sub>3</sub>X to S<sub>N</sub>2 for PdCl<sup>−</sup> + CH<sub>3</sub>X. Note, in connection with the former issue, that the activation strain increases in all cases going from TS<sub>OxIn</sub> to TS<sub>S<sub>N</sub>2-ra</sub>. We mentioned already that this is caused by the higher extent of deformation that the substrate undergoes in the S<sub>N</sub>2 and, especially, the S<sub>N</sub>2-ra transition states in which the C–X bond is essentially completely broken (see Figure 2). Interestingly, the activation strain can become even larger than the C–X bond dissociation energy. For example, the activation strain  $\Delta E_{\text{strain}}^{\ddagger}$  of 62.3 kcal/mol associated with the S<sub>N</sub>2-ra reaction of Pd + CH<sub>3</sub>At (see Table 5) is more than 7 kcal/mol higher than the CH<sub>3</sub>–At bond dissociation energy of 55.9 kcal/mol (see Table 4). The origin of this phenomenon is that, in the transition state TS<sub>S<sub>N</sub>2-ra</sub>, the methyl group stemming from the substrate remains pyramidal with an average H–C–H angle of 111° (in CH<sub>3</sub>At, the H–C–H angle is 107°), while in a straight bond dissociation reaction, the methyl group would adopt its own planar equilibrium geometry with a H–C–H angle of 120°.

Finally, we address the phenomenon that anion assistance (i.e., going from Pd to PdCl<sup>−</sup>) shifts the preference from the OxIn to the S<sub>N</sub>2 mechanism. This happens as anion assistance stabilizes the transition states of both pathways, but it does so significantly more effectively for the latter. What happens is the following: The S<sub>N</sub>2 pathway has in all cases a significantly higher, that is, less favorable, activation strain  $\Delta E_{\text{strain}}^{\ddagger}$  than the OxIn pathway. The activation strain  $\Delta E_{\text{strain}}^{\ddagger}$  is a characteristic of each of the two pathways: for each C–X bond, the activation strain is higher for TS<sub>S<sub>N</sub>2-ra</sub> than for TS<sub>OxIn</sub> because the former is inherently more distorted than the latter, in which the C–X has to elongate only slightly. Importantly, the activation strain  $\Delta E_{\text{strain}}^{\ddagger}$  changes comparatively little if we add a chloride ligand on Pd or solvent on the reaction system (see Table 5). However, the TS interaction  $\Delta E_{\text{int}}^{\ddagger}$  does change significantly. Coordination of the chloride anion effectively pushes up the palladium 4d AOs, which leads in most of the reactions to an increase of the metal–substrate TS interaction  $\Delta E_{\text{int}}^{\ddagger}$  by roughly a factor 2. In absolute terms, this means a much larger stabilization of TS<sub>S<sub>N</sub>2-ra</sub> because, in this transition state,  $\Delta E_{\text{int}}^{\ddagger}$  was already larger. The reason is the higher extent of deformation of the substrate in TS<sub>S<sub>N</sub>2-ra</sub>, in particular, the larger C–X bond expansion (see Table 1). This stabilizes the substrate  $\sigma_{\text{C-X}}^*$  LUMO and thus reinforces the metal–substrate interaction in TS<sub>S<sub>N</sub>2-ra</sub> as compared to TS<sub>OxIn</sub>. Thus,

the TS interaction always favors S<sub>N</sub>2-ra, but in the Pd-induced reactions, it is too weak to counteract the unfavorable  $\Delta E_{\text{strain}}^{\ddagger}$ . This changes in the case of the PdCl<sup>−</sup>-induced reactions in which  $\Delta E_{\text{int}}^{\ddagger}$  becomes large enough to overrule the trend in  $\Delta E_{\text{strain}}^{\ddagger}$  (which favors OxIn) and to shift the reactivity to S<sub>N</sub>2.

In the Pd + CH<sub>3</sub>Br reactions, for example, the OxIn barrier (−6 kcal/mol) is lower than the S<sub>N</sub>2-ra barrier (17 kcal/mol) because of a significantly lower activation strain for the less distortive OxIn reaction, that is, 7 versus 76 kcal/mol (see Table 5, relativistic in gas phase). The corresponding TS interactions of −13 and −60 kcal/mol, respectively, are too small to change the order set by the activation strain. Switching on anion assistance (i.e., going to PdCl<sup>−</sup> + CH<sub>3</sub>Br) has little effect on the activation strain values which go from 7 to 13 kcal/mol (OxIn) and from 76 to 79 kcal/mol (S<sub>N</sub>2-ra). However, the corresponding TS interactions jump from −13 to −24 kcal/mol (OxIn) and from −60 to −102 kcal/mol (S<sub>N</sub>2-ra). The in absolute terms larger stabilization of  $\Delta E_{\text{int}}^{\ddagger}$  in TS<sub>S<sub>N</sub>2-ra</sub> causes this transition state to drop below TS<sub>OxIn</sub>.

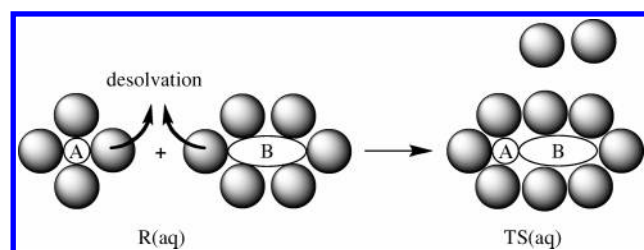
In conclusion, the heights of reaction barriers for C–X bond activation decrease as the C–X bond becomes weaker along X = F, Cl, Br, I, and At, because of the concomitant decrease in activation strain. The latter is furthermore significantly lower for the OxIn pathway, which therefore has a lower barrier and dominates the S<sub>N</sub>2 pathway in the Pd-induced reactions. Anion assistance in the PdCl<sup>−</sup>-induced reactions significantly amplifies the TS interaction which favors the S<sub>N</sub>2 pathway. This provides us with a rational approach toward tuning the stereochemistry of the C\*–X bond activation process from retention (OxIn) to inversion of configuration (S<sub>N</sub>2), simply by increasing the TS interaction with the help of a chloride ligand (see also Scheme 1).

**3.5. Activation Strain Model for Condensed-Phase Reactions.** Solvation, as pointed out above, pronouncedly changes the intrinsic reactivity trends of C–X bond activation: it causes the neutral reactions of Pd + CH<sub>3</sub>X to shift from OxIn to S<sub>N</sub>2 (for the *smaller* halogens, F and Cl) and the anion-assisted reactions of PdCl<sup>−</sup> + CH<sub>3</sub>X from S<sub>N</sub>2 to OxIn (for the *heavier* halogens, I and At; see Figure 4). In the following, we aim to understand these solvent effects on the reactivity and stereochemical selectivity of catalytic C–X bond activation, using again the conceptual framework provided by the activation strain model. In this way, the height of reaction barriers is again described and understood in terms of the rigidity and bonding capabilities of the reactants, that is, the reactants *in solution*. This enables a consistent comparison with the activation strain analyses of the gas-phase reactions. Thus, the activation energy in water,  $\Delta E^{\ddagger}(\text{aq})$ , is decomposed into the activation strain of the model catalyst and substrate in water,  $\Delta E_{\text{strain}}^{\ddagger}(\text{aq})$ , plus the corresponding metal–substrate interaction in water,  $\Delta E_{\text{int}}^{\ddagger}(\text{aq})$ :

$$\Delta E^{\ddagger}(\text{aq}) = \Delta E_{\text{strain}}^{\ddagger}(\text{aq}) + \Delta E_{\text{int}}^{\ddagger}(\text{aq}) \quad (3)$$

Note that both  $\Delta E_{\text{strain}}^{\ddagger}(\text{aq})$  and  $\Delta E_{\text{int}}^{\ddagger}(\text{aq})$  contain effects due to solvation. The activation strain in solution,  $\Delta E_{\text{strain}}^{\ddagger}(\text{aq})$ ,



**Scheme 2.** Desolvation of Fragments A and B When Complex AB Is Formed

is the energy associated with deforming the reactants from their equilibrium structure *in solution* to the geometry they adopt in the TS *in solution*. To reveal which role the solvent plays in this term, the latter is decomposed into three terms (eq 4): (i) the pure deformation energy, that is, the change in energy associated with the geometrical deformation of the reactants in solution *but in the absence of the solvent*,  $\Delta E_{\text{strain,pure}}^{\ddagger}$ ; (ii) the change in cavitation energy associated with the corresponding deformation of the cavity in the solvent that houses the reactants,  $\Delta E_{\text{strain,cav}}^{\ddagger}$ ; and (iii) the corresponding change in solute–solvent interaction, that is, in solvation stabilization  $\Delta E_{\text{strain,solv}}^{\ddagger}$ :

$$\Delta E_{\text{strain}}^{\ddagger}(\text{aq}) = \Delta E_{\text{strain,pure}}^{\ddagger} + \Delta E_{\text{strain,cav}}^{\ddagger} + \Delta E_{\text{strain,solv}}^{\ddagger} \quad (4)$$

Thus, the activation strain in water depends on the rigidity of the reactants (mainly the substrate), the extent to which the solvent cavities must change in reaction to the geometrical deformation of the reactants, and the effect of all these geometrical deformations of reactants and solvent on the solute–solvent interaction.

The TS interaction in solution,  $\Delta E_{\text{int}}^{\ddagger}(\text{aq})$ , is the energy associated with bringing the deformed reactants *in solution* together in the TS *in solution*. To also uncover how the solvent affects this term,  $\Delta E_{\text{int}}^{\ddagger}(\text{aq})$  is decomposed again into three terms (eq 5): (i) the change in energy associated with the desolvation of those sites on either reactant that in the TS are bonding and/or in steric contact,  $\Delta E_{\text{int,desolv}}^{\ddagger}$ , see also Scheme 2; (ii) the change in cavitation energy associated with going from two reactant cavities in the solvent to one cavity that houses the TS,  $\Delta E_{\text{int,cav}}^{\ddagger}$ ; and (iii) the pure interaction energy between the partially desolvated reactants (i.e., without desolvation and cavitation effects),  $\Delta E_{\text{int,pure}}^{\ddagger}$ :

$$\Delta E_{\text{int}}^{\ddagger}(\text{aq}) = \Delta E_{\text{int,desolv}}^{\ddagger} + \Delta E_{\text{int,cav}}^{\ddagger} + \Delta E_{\text{int,pure}}^{\ddagger} \quad (5)$$

The  $\Delta E_{\text{int,desolv}}^{\ddagger}$  is computed as the change in solute–solvent interaction when each of the deformed reactants is brought from its regular cavity to the TS cavity *in the absence of the other reactant* (i.e., by using ghost atoms for the other reactant). The term  $\Delta E_{\text{int,pure}}^{\ddagger}$  is then computed as  $\Delta E_{\text{int}}^{\ddagger}(\text{aq}) - \Delta E_{\text{int,desolv}}^{\ddagger} - \Delta E_{\text{int,cav}}^{\ddagger}$ .

**3.6. Activation Strain Analysis of Condensed-Phase Reactivity.** Solvation shifts the preference of the neutral Pd + CH<sub>3</sub>X reactions from OxIn to S<sub>N</sub>2 (see Table 5) for two reasons: (i) it weakens the C–X bond regarding heterolytic bond cleavage and thus effectively reduces the rigidity of the substrate, and (ii) it stabilizes the metal–substrate interaction by the concomitant enhancement of the charge

separation C<sup>δ+</sup>–X<sup>δ-</sup> in the substrate. This shows up in a lower activation strain in water,  $\Delta E_{\text{strain}}^{\ddagger}(\text{aq})$ , as compared to that in the gas phase,  $\Delta E_{\text{strain}}^{\ddagger}$ , as well as in a more stabilizing TS interaction in water,  $\Delta E_{\text{int}}^{\ddagger}(\text{aq})$ , as compared to that in the gas phase,  $\Delta E_{\text{int}}^{\ddagger}$  (see Table 5). Importantly, this stabilizing effect is stronger for the more deformed TS<sub>S<sub>N</sub>2-ra</sub> than for TS<sub>OxIn</sub> as the former has a significantly more elongated and polarized C<sup>δ+</sup>–X<sup>δ-</sup> bond (vide supra). In the case of Pd + CH<sub>3</sub>Cl, for example, hydration stabilizes the activation strain and TS interaction of the OxIn pathway by only 0.0 and –2.1 kcal/mol, respectively, whereas it stabilizes the corresponding terms of the S<sub>N</sub>2-ra reaction by a sizable –7.3 and –20.1 kcal/mol, respectively [Table 5: compare  $\Delta E_{\text{strain}}^{\ddagger}(\text{aq})$  with  $\Delta E_{\text{strain}}^{\ddagger}$  and  $\Delta E_{\text{int}}^{\ddagger}(\text{aq})$  with  $\Delta E_{\text{int}}^{\ddagger}$ ]. The solvent-induced stabilization of the activation strain and TS interaction furthermore increases along At, I, Br, Cl, and F, that is, if one goes to the smaller and more electronegative halogens. Thus, for Pd + CH<sub>3</sub>I, the hydration-induced stabilization of the activation strain and TS interaction of the S<sub>N</sub>2-ra reaction has been reduced to +2 (i.e., a slight *destabilization*) and –15.3 kcal/mol, respectively. As a result, the barriers of the S<sub>N</sub>2 pathway approach those of the OxIn pathway, and for F and Cl, TS<sub>S<sub>N</sub>2-ra</sub> becomes lower in energy than TS<sub>OxIn</sub>.

Further analyses show that the hydration-induced stabilization of the activation strain in the case of the smaller halogens is indeed caused by a better solvation term,  $\Delta E_{\text{strain,solv}}^{\ddagger}$ . In the case of the S<sub>N</sub>2-ra reaction, the latter amounts to –19.9 (F), –10.8 (Cl), –3.2 (Br), +4.4 (I), and +6.7 kcal/mol (At) (see Table 5). The cavitation term,  $\Delta E_{\text{strain,cav}}^{\ddagger}$ , is nowhere larger than a virtually negligible 0.1 kcal/mol. The reason for the large solvent stabilization in the case of TS<sub>S<sub>N</sub>2-ra</sub> is that solvation in water stabilizes charge separation and opens the possibility for heterolytic bond dissociation of the CH<sub>3</sub>–X bond, that is, dissociation into the ionic fragments CH<sub>3</sub><sup>+</sup> and X<sup>–</sup>. This is nicely illustrated by the data in Table 4, which shows homolytic and heterolytic C–X bond dissociation energies for both the gas phase and the water phase. In the gas phase, the homolytic C–X dissociation is always more favorable than the heterolytic one. But, in water, heterolytic dissociation is significantly more strongly stabilized. In the case of F and Cl, heterolytic dissociation becomes even more favorable than homolytic dissociation. In the cases of Br, I, and At, the selective stabilization of the heterolytic C–X dissociation is not strong enough to open this ionic dissociation mode as a more favorable alternative to homolytic dissociation.

The above effects of hydration on the activation strain can be easily understood with the classical electrostatic Born model of a spherical ion in a dielectric continuum (eq 6):<sup>43</sup>

$$\Delta E_{\text{solv}} = -\frac{q^2}{8\pi\epsilon_0 a} \left(1 - \frac{1}{\epsilon_r}\right) \quad (6)$$

In this equation,  $\epsilon_0$  is the dielectric constant in a vacuum and  $\epsilon_r$  is the relative dielectric constant of the solvent (i.e., 78.4 for water). The charge  $q$  is –1 for the X<sup>–</sup> ion. The appearance of the radius  $a$  of the ion in the denominator leads to smaller solvation energies for larger ions. On the



basis of this simple model, it is immediately clear why the dissociation of  $\text{CH}_3\text{X}$  into  $\text{CH}_3^+$  and  $\text{X}^-$  in water is more favored for the smaller halogens: the large halogenide anions are in a sense too large to be well-stabilized by solvation.

Likewise, further analyses show that the hydration-induced stabilization of the TS interaction in the case of the smaller halogens is indeed caused by a reinforcement of the pure interaction between the solvated reactants,  $\Delta E_{\text{int,pure}}^\ddagger$ , which dominates all other effects (Table 5: compare this term directly with  $\Delta E_{\text{int}}^\ddagger$  or  $\Delta E_{\text{int,gas}}^\ddagger$ ). The contribution of the changing cavitation energy  $\Delta E_{\text{int,cav}}^\ddagger$  is in all cases small, that is, around  $-1.5$  kcal/mol (Table 5). This decrease in cavitation energy is caused by the fact that the deformed reactants occupy less space when they form the complex than when they are apart from each other. The partial desolvation energy  $\Delta E_{\text{int,desolv}}^\ddagger$  is (naturally) always destabilizing.

Finally, we extend our analysis to the anion-assisted  $\text{PdCl}^- + \text{CH}_3\text{X}$  reactions in water to understand why here solvation shifts the reactivity from  $\text{S}_{\text{N}}2$  to OxIn, that is, in the opposite direction as compared to the effect of solvation on the neutral reactions. The main effect of solvation appears to be the *weakening* of the metal–substrate TS interaction, at variance with the strengthening in the case of the neutral reactions  $\text{Pd} + \text{CH}_3\text{X}$  (vide infra). On the other hand, the activation strain behaves quite similar in the anion-assisted and neutral reactions, since the substrates are identical and the strain in Pd and  $\text{PdCl}^-$  is zero versus negligible.

The TS interaction, as discussed above, is more stabilizing for the  $\text{S}_{\text{N}}2$  pathway and therefore favors this mechanism over OxIn. In the gas phase, anion assistance amplifies the TS interaction term, which causes the reactivity to switch from OxIn, for  $\text{Pd} + \text{CH}_3\text{X}$ , to  $\text{S}_{\text{N}}2$ , for  $\text{PdCl}^- + \text{CH}_3\text{X}$  (see Figure 4 and Table 5). Now, if we go from the gas phase to the water phase, the TS interaction becomes again weaker, an effect that favors the OxIn transition states because it destabilizes the barrier of the anion-assisted  $\text{TS}_{\text{S}_{\text{N}}2-\text{ra}}$  more than that of the corresponding  $\text{TS}_{\text{OxIn}}$ . For example, for the neutral  $\text{Pd} + \text{CH}_3\text{At}$  reaction, solvation *strengthens* the TS interaction of  $\text{TS}_{\text{OxIn}}$  and  $\text{TS}_{\text{S}_{\text{N}}2-\text{ra}}$  by  $-2.6$  and  $-13.4$  kcal/mol, respectively, while for the anion-assisted  $\text{PdCl}^- + \text{CH}_3\text{-At}$  reaction, solvation *weakens* the TS interaction of  $\text{TS}_{\text{OxIn}}$  and  $\text{TS}_{\text{S}_{\text{N}}2-\text{ra}}$  by  $+7.0$  and  $+10.3$  kcal/mol, respectively (Table 5: compare  $\Delta E_{\text{int}}^\ddagger(\text{aq})$  with  $\Delta E_{\text{int}}^\ddagger$  values).

Similar solvent effects occur for the barrier associated with  $\text{TS}_{\text{S}_{\text{N}}2}$  which, in the case of  $\text{X} = \text{I}$  and  $\text{At}$ , becomes even higher in energy than that with  $\text{TS}_{\text{OxIn}}$  (see Figure 4 and Table 5). But the similarity between the solvent effects in the precise electronic mechanism through which solvation destabilizes both  $\text{TS}_{\text{S}_{\text{N}}2}$  and  $\text{TS}_{\text{S}_{\text{N}}2-\text{ra}}$  is masked by the relatively large concomitant shift, along the reaction coordinate of the former, toward the product side. As explained in detail in ref 10, this brings the solvated  $\text{TS}_{\text{S}_{\text{N}}2-\text{ra}}$  to a position on the reaction coordinate at which interactions are much stronger, and this, in turn, masks the solvation-induced weakening of the TS interaction. In addition, a direct comparison between the gas-phase and water-phase  $\text{TS}_{\text{S}_{\text{N}}2}$  is further complicated by the fact that for  $\text{PdCl}^- + \text{CH}_3\text{X}$  this transition state exists only for  $\text{X} = \text{F}$  and  $\text{Cl}$  but not for the other halogens. To nevertheless enable a systematic gas-

phase versus condensed-phase comparison, we have also computed the TS interaction in all the *condensed-phase*  $\text{TS}_{\text{S}_{\text{N}}2}$  geometries, *however, in the absence of solvent*. The metal–substrate interaction associated with this structure is designated  $\Delta E_{\text{int,gas}}^\ddagger$  and serves as a measure for the gas-phase TS interaction  $\Delta E_{\text{int}}^\ddagger$ . Moreover,  $\Delta E_{\text{int,gas}}^\ddagger$  serves as a point of reference to which the condensed-phase TS interaction  $\Delta E_{\text{int}}^\ddagger(\text{aq})$  can be compared in a consistent fashion, that is, without strong geometry effects that mask the intrinsic change in the interaction. Indeed, the values of the condensed-phase TS interaction  $\Delta E_{\text{int}}^\ddagger(\text{aq})$  of  $-22$  to  $-37$  kcal/mol are substantially less stabilizing than those of  $\Delta E_{\text{int,gas}}^\ddagger$  of  $-36$  to  $-50$  kcal/mol (see Table 5).

Further analyses show that the hydration-induced weakening of the TS interaction of the anion-assisted  $\text{PdCl}^- + \text{CH}_3\text{X}$  reactions is, in most cases, mainly caused by a weakening of the pure interaction between the solvated reactants,  $\Delta E_{\text{int,pure}}^\ddagger$ , which dominates all other effects (Table 5: compare this term directly with  $\Delta E_{\text{int}}^\ddagger$  or  $\Delta E_{\text{int,gas}}^\ddagger$ ). The contribution of the changing cavitation energy  $\Delta E_{\text{int,cav}}^\ddagger$  is in all cases small, that is, around  $-1.5$  kcal/mol (Table 5). This decrease in cavitation energy is caused by the fact that the deformed reactants occupy less space when they form the complex than when they are apart from each other. The partial desolvation energy  $\Delta E_{\text{int,desolv}}^\ddagger$  is (naturally) always destabilizing but relatively unimportant, that is, about 1 order of magnitude smaller than  $\Delta E_{\text{int,pure}}^\ddagger$  (see Table 5). The hydration-induced weakening of the pure metal–substrate interaction is ascribed to the polarization of the negative charge on  $\text{PdCl}^-$  (away from the desolvated binding site) and the stabilization of the highest occupied molecular orbitals on  $\text{PdCl}^-$ , which reduces the capability of these orbitals to participate in donor–acceptor orbital interactions. Similar effects have been analyzed in detail for the E2 and  $\text{S}_{\text{N}}2$  reactions of  $\text{F}^- + \text{CH}_3\text{CH}_2\text{F}$ .<sup>31</sup>

## 4. Conclusions

Palladium-catalyzed  $\text{C}^*-\text{X}$  bond activation in halomethanes can proceed through two stereochemically different pathways: direct oxidative insertion (OxIn, which goes with the retention of configuration at  $\text{C}^*$ ) and  $\text{S}_{\text{N}}2$  substitution (which goes with the inversion of configuration at  $\text{C}^*$ ). Using the activation strain model of chemical reactivity, we have shown that the barriers of all pathways decrease along  $\text{X} = \text{F}, \text{Cl}, \text{Br}, \text{I},$  and  $\text{At}$  because the  $\text{C}-\text{X}$  bond becomes less stable and therefore less rigid along this series. Relativistic effects substantially stabilize the stationary points along the PES, but they do not change the relative order in barrier heights and reaction energies along the various model reactions.

Interestingly, our activation strain analyses provide a very simple and transparent picture of how anion assistance (i.e., going from the model catalyst Pd to  $\text{PdCl}^-$ ) and solvation (water, described through the COSMO model) affect the overall reactivity and the selectivity between the OxIn (retention of configuration) and  $\text{S}_{\text{N}}2$  pathways (inversion of configuration). The latter pathway is inherently connected with a higher extent of deformation of the substrate in the TS, which leads to a higher activation strain  $\Delta E_{\text{strain}}^\ddagger$  for  $\text{S}_{\text{N}}2$  than for OxIn. Through the relationship  $\Delta E^\ddagger = \Delta E_{\text{strain}}^\ddagger +$

$\Delta E_{\text{int}}^{\ddagger}$ , this contributes to a higher reaction barrier  $\Delta E^{\ddagger}$  for  $S_N2$  than for OxIn.

This situation can now be modulated by the TS interaction  $\Delta E_{\text{int}}^{\ddagger}$  which favors the  $S_N2$  pathway because the more deformed substrate in the latter is also a better partner in electrostatic and donor–acceptor orbital interactions. Thus, whenever the TS interaction  $\Delta E_{\text{int}}^{\ddagger}$  is small, the trend in selectivity is determined more by the activation strain  $\Delta E_{\text{strain}}^{\ddagger}$ , and vice versa.

Thus, anion assistance, which increases the bonding capabilities of the model catalyst, favors the  $S_N2$  pathway. On the other hand, solvation on top of anion assistance diminishes the bonding capabilities of the model catalyst and therefore favors again the OxIn pathway.

**Acknowledgment.** We thank the Nederlandse Organisatie voor Wetenschappelijk Onderzoek (NWO-CW and NWO-NCF) for financial support.

**Supporting Information Available:** Energies with zero-point vibrational energy corrections and enthalpies at 298.15 K of all stationary points at all levels of theory and Cartesian coordinates of all species occurring in this study. This material is available free of charge via the Internet at <http://pubs.acs.org>.

## References

- (1) Collman, J. P.; Hegedus, L. S.; Norton, J. R.; Finke, R. G. *Principles and Applications of Organotransition Metal Chemistry*; University Science Books: Mill Valley, California, 1987. Elschenbroich, Ch. A. *Organometallics*; Wiley-VCH: Weinheim, Germany, 2006.
- (2) Grushin, V. V.; Alper, H. *Chem. Rev.* **1994**, *94*, 1047. Amatore, C.; Jutand, A. *Acc. Chem. Res.* **2000**, *33*, 314.
- (3) Luh, T.-Y.; Leung, M.-k.; Wong, K. T. *Chem. Rev.* **2000**, *100*, 3187.
- (4) Ritter, D.; Weisshaar, J. C. *J. Am. Chem. Soc.* **1990**, *112*, 6425. Fayet, P.; Kaldor, A.; Cox, D. M. *J. Chem. Phys.* **1990**, *92*, 254. Carroll, J. J.; Weisshaar, J. C. *J. Am. Chem. Soc.* **1993**, *115*, 800. Casado, A. L.; Espinet, P. *Organometallics* **1998**, *17*, 954. Stürmer, R. *Angew. Chem.* **1999**, *111*, 3509. Hinrichs, R. Z.; Schroden, J. J.; Davis, H. F. *J. Am. Chem. Soc.* **2003**, *125*, 860. de Pater, B. C.; Zijp, E. J.; Frühauf, H.-W.; Ernsting, J. M.; Elsevier, C. J.; Vrieze, K. *Organometallics* **2004**, *23*, 269. Espinet, P.; Echavarren, A. *Angew. Chem.* **2004**, *116*, 4808. Wang, G.; Chen, M.; Zhou, M. *Chem. Phys. Lett.* **2005**, *412*, 46. Lersch, M.; Tilset, M. *Chem. Rev.* **2005**, *105*, 2471.
- (5) Weisshaar, J. C. *Acc. Chem. Res.* **1993**, *26*, 213. Carroll, J. J.; Haug, K. L.; Weisshaar, J. C.; Blomberg, M. R. A.; Siegbahn, P. E. M.; Svensson, M. *J. Phys. Chem.* **1995**, *99*, 13955. Porembski, M.; Weisshaar, J. C. *J. Phys. Chem. A* **2000**, *104*, 1524. Haynes, A.; Maitlis, P. M.; Morris, G. E.; Sunley, G. J.; Adams, H.; Badger, P. W.; Bowers, C. M.; Cook, D. B.; Elliott, P. I. P.; Ghaffar, T.; Green, H.; Griffin, T. R.; Payne, M.; Pearson, J. M.; Taylor, M. J.; Vickers, P. W.; Watt, R. J. *J. Am. Chem. Soc.* **2004**, *126*, 2847.
- (6) Siegbahn, P. E. M.; Blomberg, M. R. A.; Svensson, M. *J. Am. Chem. Soc.* **1993**, *115*, 1952. Griffin, T. R.; Cook, D. B.; Haynes, A.; Pearson, J. M.; Monti, D.; Morris, G. E. *J. Am. Chem. Soc.* **1996**, *118*, 3029. Siegbahn, P. E. M. *J. Am. Chem. Soc.* **1996**, *118*, 1487. Wittborn, A. M. C.; Costas, M.; Blomberg, M. R. A.; Siegbahn, P. E. M. *J. Chem. Phys.* **1997**, *107*, 4318. Cui, Q.; Musaev, D. G.; Morokuma, K. *J. Chem. Phys.* **1998**, *108*, 8418. Torrent, M.; Solà, M.; Frenking, G. *Chem. Rev.* **2000**, *100*, 439. Senn, H. M.; Ziegler, T. *Organometallics* **2004**, *23*, 2980. Gooßen, L. J.; Koley, D.; Hermann, H.; Thiel, W. *Chem. Commun.* **2004**, 2141. Kozuch, S.; Shaik, S.; Jutand, A.; Amatore, C. *Chem.—Eur. J.* **2004**, *10*, 3072. Diefenbach, A.; Bickelhaupt, F. M. *J. Organomet. Chem.* **2005**, *690*, 2191. de Jong, G. Th.; Visser, R.; Bickelhaupt, F. M. *J. Organomet. Chem.* **2006**, *691*, 4341.
- (7) Diefenbach, A.; Bickelhaupt, F. M. *J. Chem. Phys.* **2001**, *115*, 4030.
- (8) de Jong, G. Th.; Solà, M.; Visscher, L.; Bickelhaupt, F. M. *J. Chem. Phys.* **2004**, *121*, 9982.
- (9) Diefenbach, A.; de Jong, G. Th.; Bickelhaupt, F. M. *Mol. Phys.* **2005**, *103*, 995.
- (10) Diefenbach, A.; de Jong, G. Th.; Bickelhaupt, F. M. *J. Chem. Theory Comput.* **2005**, *1*, 286.
- (11) de Jong, G. Th.; Geerke, D. P.; Diefenbach, A.; Bickelhaupt, F. M. *Chem. Phys.* **2005**, *313*, 261.
- (12) de Jong, G. Th.; Geerke, D. P.; Diefenbach, A.; Solà, M.; Bickelhaupt, F. M. *J. Comput. Chem.* **2005**, *26*, 1006.
- (13) de Jong, G. Th.; Bickelhaupt, F. M. *J. Phys. Chem. A* **2005**, *109*, 9685.
- (14) de Jong, G. Th.; Bickelhaupt, F. M. *J. Chem. Theory Comput.* **2006**, *2*, 322.
- (15) March, J. *Advanced Organic Chemistry*; McGraw-Hill: Tokyo, 1977. Dedieu, A. *Chem. Rev.* **2000**, *100*, 543. Nicolaou, K. C.; Bulger, P. G.; Sarlah, D. *Angew. Chem.* **2005**, *117*, 4516.
- (16) Frisch, A. C.; Beller, M. *Angew. Chem.* **2005**, *117*, 680.
- (17) Kiplinger, J. L.; Richmond, Th. G.; Osterberg, C. E. *Chem. Rev.* **1994**, *94*, 373.
- (18) Bickelhaupt, F. M.; Ziegler, T.; von Ragué Schleyer, P. *Organometallics* **1995**, *14*, 2288.
- (19) Bickelhaupt, F. M. *J. Comput. Chem.* **1999**, *20*, 114.
- (20) Hohenberg, P.; Kohn, W. *Phys. Rev.* **1964**, *136*, B864. Kohn, W.; Sham, L. J. *Phys. Rev.* **1965**, *140*, A1133. Parr, R. G.; Yang, W. *Density-Functional Theory of Atoms and Molecules*; Oxford University Press: New York, 1989.
- (21) Baerends, E. J.; Ellis, D. E.; Ros, P. *Chem. Phys.* **1973**, *2*, 41.
- (22) te Velde, G.; Bickelhaupt, F. M.; Baerends, E. J.; Fonseca Guerra, C.; van Gisbergen, S. J. A.; Snijders, J. G.; Ziegler, T. *J. Comput. Chem.* **2001**, *22*, 931. Baerends, E. J.; Autschbach, J.; Bérces, A.; Bo, C.; Boerrigter, P. M.; Cavallo, L.; Chong, D. P.; Deng, L.; Dickson, R. M.; Ellis, D. E.; van Faassen, M.; Fan, L.; Fischer, T. H.; Fonseca Guerra, C.; van Gisbergen, S. J. A.; Groeneveld, J. A.; Gritsenko, O. V.; Grüning, M.; Harris, F. E.; van den Hoek, P.; Jacobsen, H.; Jensen, L.; van Kessel, G.; Kootstra, F.; van Lenthe, E.; McCormack, D. A.; Michalak, A.; Osinga, V. P.; Patchkovskii, S.; Philipsen, P. H. T.; Post, D.; Pye, C. C.; Ravenek, W.; Ros, P.; Schipper, P. R. T.; Schreckenbach, G.; Snijders, J. G.; Solà, M.; Swart, M.; Swerhone, D.; te Velde, G.; Vernooijs, P.; Versluis, L.; Visser, O.; Wang, F.; van Wezenbeek, E.; Wiesenekker, G.; Wolff, S. K.; Woo, T. K.; Yakovlev, A. L.; Ziegler, T. *ADF2005.01*; SCM, Theoretical Chemistry: Vrije Universiteit, Amsterdam, The Netherlands, 2005.

- (23) van Lenthe, E.; Baerends, E. J.; Snijders, J. G. *J. Chem. Phys.* **1994**, *101*, 9783.
- (24) Becke, A. D. *Phys. Rev. A: At., Mol., Opt. Phys.* **1988**, *38*, 3098. Lee, C.; Yang, W.; Parr, R. G. *Phys. Rev. B: Condens. Matter Mater. Phys.* **1988**, *37*, 785.
- (25) Bickelhaupt, F. M.; Baerends, E. J. Kohn-Sham Density Functional Theory: Predicting and Understanding Chemistry. In *Reviews in Computational Chemistry*; Lipkowitz, K. B., Boyd, D. B., Eds.; VCH Publishers Inc.: New York, 2000; Vol. 15; p 1.
- (26) Klamt, A.; Schüürmann, G. *J. Chem. Soc., Perkin Trans. 2* **1993**, 799. Klamt, A. *J. Phys. Chem.* **1995**, *99*, 2224.
- (27) Pye, C. C.; Ziegler, T. *Theor. Chem. Acc.* **1999**, *101*, 396.
- (28) Bon, R. S.; van Vliet, B.; Sprenkels, N. E.; Schmitz, R. F.; de Kanter, F. J. J.; Stevens, Chr. V.; Swart, M.; Bickelhaupt, F. M.; Groen, M. B.; Orru, R. V. A. *J. Org. Chem.* **2005**, *70*, 3542.
- (29) Allinger, N. L.; Zhou, X.; Bergsma, J. *THEOCHEM* **1994**, *312*, 69.
- (30) van Duijnen, P. T.; Grozema, F. C.; Swart, M. *THEOCHEM* **1999**, *464*, 191.
- (31) Bickelhaupt, F. M.; Baerends, E. J.; Nibbering, N. M. M. *Chem.—Eur. J.* **1996**, *2*, 196.
- (32) Cizek, J. *J. Chem. Phys.* **1966**, *45*, 4256. Purvis, G. D., III; Bartlett, R. J. *J. Chem. Phys.* **1982**, *76*, 1910. Raghavachari, K.; Trucks, G. W.; Pople, J. A.; Head-Gordon, M. *Chem. Phys. Lett.* **1989**, *157*, 479.
- (33) Visscher, L.; Lee, T. J.; Dyall, K. G. *J. Chem. Phys.* **1996**, *105*, 8769. Jensen, H. J. Aa.; Saue, T.; Visscher, L. *DIRAC*, version 4.0; Syddansk Universitet: Odense, Denmark, 2004.
- (34) Lévy-Leblond, J. M. *Commun. Math. Phys.* **1967**, *6*, 286.
- (35) Dyall, K. G. *J. Chem. Phys.* **1994**, *100*, 2118.
- (36) Visscher, L. *Theor. Chem. Acc.* **1997**, *98*, 68.
- (37) Kendall, R. A.; Dunning, Th. H., Jr.; Harrison, R. J. *J. Chem. Phys.* **1992**, *96*, 6796.
- (38) Dyall, K. *Theor. Chem. Acc.* **2002**, *108*, 335.
- (39) de Jong, G. Th.; Kovács, A.; Bickelhaupt, F. M. *J. Phys. Chem. A* **2006**, *110*, 7943.
- (40) Deng, L.; Branchadell, V.; Ziegler, T. *J. Am. Chem. Soc.* **1994**, *116*, 10645.
- (41) Linstrom, J.; Mallard, W. G. P. *NIST Standard Reference Database Number 69*, June 2005 Release. <http://webbook.nist.gov/chemistry> (accessed Jul 2006).
- (42) For example, the relativistic energy including spin–orbit coupling of the oxidative-addition product P of Pd + CH<sub>3</sub>–At relative to R is –45.1 kcal/mol (not shown in a table), which differs only 2.4 kcal/mol from the scalar relativistic value of –42.7 kcal/mol (see Table 3).
- (43) Born, M. Z. *Phys.* **1920**, *1*, 45. Atkins, P. W. *Physical Chemistry*; Oxford University Press: Oxford, United Kingdom, 1994.

CT600342J